Earliest human burial in Africa

María Martinón-Torres[1,2]*, Francesco d'Errico[3,4], Elena Santos[5,6], Ana Álvaro Gallo[1], Noel Amano[7], William Archer[8,9,10], Simon J. Armitage[11,4], Juan Luis Arsuaga[5,12], José María Bermúdez de Castro[1,2], James Blinkhorn[13,11,7], Alison Crowther[7,14], Katerina Douka[7,15], Stéphan Dubernet[16], Patrick Faulkner[17,6], Pilar Fernández-Colón[1], Nikos Kourampas[18,19], Jorge González García[20], David Larreina[1], François-Xavier Le Bourdonnec[16], George MacLeod[19], Laura Martín-Francés[1], Diyendo Massilani[21], Julio Mercader[22,6], Jennifer M. Miller[7], Emmanuel Ndiema[23,7], Belén Notario[1], Africa Pitarch Martí[3,24], Mary E. Prendergast[25], Alain Queffelec[3], Solange Rigaud[3], Patrick Roberts[7,14], Mohammad Javad Shoaee[7], Ceri Shipton[26,27], Ian Simpson[18], Nicole Boivin[7,14,22,28]* & Michael D. Petraglia[7,14,29,30]*

[1]CENIEH (National Research Center on Human Evolution), Paseo de la Sierra de Atapuerca 3, 09002, Burgos, Spain.

[2]Anthropology Department, University College London, 14 Taviton Street, London WC1H 0BW, UK.

[3]UMR 5199 CNRS De la Préhistoire à l'Actuel: Culture, Environnement, et Anthropologie (PACEA), Université Bordeaux, Allée Geoffroy Saint Hilaire, CS 50023 F - 33615 Pessac CEDEX, Talence, France.

[4]SFF Centre for Early Sapiens Behaviour (SapienCE), University of Bergen, Post Box 7805, 5020, Bergen, Norway.

[5]Centro Mixto UCM-ISCIII de Evolución y Comportamiento Humanos, Instituto de Salud Carlos III, 28029, Madrid, Spain.

[6]Cátedra de Otoacústica Evolutiva y Paleoantropología (HM Hospitales - Universidad de Alcalá). Departamento de Ciencias de la Vida, Universidad de Alcalá (Spain).

[7]Department of Archaeology, Max Planck Institute for the Science of Human History, Kahlaische Strasse, 07745, Jena, Germany.

[8]Department of Archaeology and Anthropology, National Museum, Bloemfontein, South Africa.

[9]Department of Archaeology, University of Cape Town, South Africa.

[10]Department of Human Evolution, Max Planck Institute for Evolutionary Anthropology, Leipzig, Germany.

[11]Department of Geography, Royal Holloway, University of London, Egham, Surrey, TW20 OEX, UK.

[12]Departamento de Paleontología, Facultad de Ciencias Geológicas, Universidad Complutense de Madrid, 28040, Madrid, Spain.

[13]Pan-African Evolution Research Group, Max Planck Institute for the Science of Human History, Kahlaische Strasse 10, D-07745 Jena, Germany

[14]School of Social Science, The University of Queensland, St Lucia QLD 4072, Brisbane, Australia.

[15]Research Laboratory for Archaeology and the History of Art, Dyson Perrins Building, South Parks Road, Oxford, OX1 3QY, UK.

[16]UMR 5060 CNRS-Université Bordeaux Montaigne IRAMAT-CRP2A: Institut de recherche sur les Archéomatériaux – Centre de recherche en physique appliquée à l'archéologie, Maison de l'archéologie, Esplanade des Antilles, 33607 Pessac Cedex, France.

[17]Faculty of Arts and Social Sciences, Department of Archaeology, The University of Sydney, Sydney, NSW, Australia.

[18]Centre for Open Learning, University of Edinburgh, Paterson's Land, Edinburgh, EH8 8AQ, Scotland, UK.

[19]Biological and Environmental Sciences, University of Stirling, Stirling, FK9 4LA, Scotland, UK.

[20]3D Applications Engineer and Heritage Specialist Digital Heritage and Humanities Collections, University of South Florida, 4202 E. Fowler Ave., LIB 122, Tampa, Florida, USA.

[21]Department of Evolutionary Genetics, Max Planck Institute for Evolutionary Anthropology, Leipzig, Germany.

[22]Department of Anthropology and Archaeology, University of Calgary, 2500 University Drive, Calgary, AB, T2N 1N4, Canada.

[23]National Museums of Kenya, Department of Earth Sciences, Nairobi, Kenya.

[24]Seminari d'Estudis i Recerques Prehistòriques (SERP), Facultat de Geografia i Història, Departament d'Història i Arqueologia, Universitat de Barcelona, Montalegre 6, 08001, Barcelona, Spain.

[25]Department of Sociology and Anthropology, Saint Louis University, Avenida del Valle 34, Madrid, Spain.

[26]Institute of Archaeology, University College London, Gordon Square, WC1H 0PY, U.K.

[27]Centre of Excellence for Australian Biodiversity and Heritage, The Australian National University, Canberra, Australia.

[28]Department of Anthropology, National Museum of Natural History, Smithsonian Institution, Washington, D.C., 20560, USA.

[29]Human Origins Program, National Museum of Natural History, Smithsonian Institution, Washington, D.C., 20560, USA.

[30]Australian Research Centre for Human Evolution (ARCHE), Griffith University, Brisbane, Queensland, Australia.

[*] Corresponding authors

The origin and evolution of hominin mortuary practices are topics of intense interest and debate[1-3]. Human burials dated to the Middle Stone Age (MSA) are exceedingly rare in Africa and unknown in East Africa[1-6]. Here, we describe the partial skeleton of a c. 2.5-3.0 year-old child dating to 78.3 ± 4.1 ka, recovered in the MSA layers of Panga ya Saidi (PYS), a cave site in the tropical upland coast

of Kenya[7-8]. Recent excavations revealed a pit feature containing a child in a flexed position. Geochemical, granulometric and micromorphological analyses of the burial pit content and encasing archaeological layers indicate that the pit was deliberatly excavated. Taphonomical evidence such as the strict articulation or good anatomical association of the skeletal elements and histological evidence of putrefaction support the in-place decomposition of the fresh body. Absent to minimal displacement of the unstable joints during decomposition points to an interment in a filled space (grave earth) making the PYS finding the oldest human burial in Africa. The morphological assessment of the partial skeleton is consistent with its assignment to *Homo sapiens*, although the preservation of some primitive features in the dentition supports increasing evidence for non-gradual assembly of modern traits during the emergence of our species. The PYS burial sheds new light on how MSA populations interacted with the dead.

Increasing scrutiny is being placed on the origin and biological and cultural evolution of our species in Africa[1–3]. Mortuary practices are a significant component of our evolution[4–6]. Formal burials, defined as the interment of a dead body in an excavated grave, may have been preceded by more elusive practices in the genus *Homo*. Testing this scenario is made difficult, particularly in Africa, by the scarcity of sites with clear and well-dated evidence for the treatment of dead bodies.

Panga ya Saidi (PYS) has emerged as one of the key Middle Stone Age (MSA) and Later Stone Age (LSA) sites of Africa given its excellent preservation of environmental proxies[7,8], its distinctive sequence of technological innovations and symbolic traits[8,9], and its preservation of biomolecular information[10,11]. The excavated cave sequence is ~3 metres deep and encompasses 19 layers (Fig. 1). A series of

stratigraphically ordered radiocarbon and luminescence ages, when included in a Bayesian model, indicate human occupation from ~78 ka to 500 years ago[8], representing most of the last five marine isotope stages.

The 2013 excavations at PYS revealed a partial pit feature in profile, markedly contrasting with the gradual colour change that characterizes the entire sequence and presenting a distinct texture and colour in comparison to the surrounding matrix (Fig. 1, Supplementary Information A). A luminescence tube (OSL4) and a micromorphology sample (PYS 13_1) were placed in the feature. The micromorphology sample revealed the presence of heavily degraded bones. Excavations were expanded in 2017 to expose the top of the feature, which was positioned at the bottom of Layer 18. The plan view of the pit was subcircular, measuring 36.7 cm (north-south) x 39.8 cm (west-east) x 12.5 cm (depth). Limited excavation at the top of the pit indicated that the feature contained a concentration of fragile and degraded bones in association with MSA lithic artefacts (Extended Data Fig. 1, Supplementary Information B), embedded in a matrix different from the surrounding sediments of Layer 19. The excavation surface indicated the presence of decomposed bones that were later shown to be the base of a skull and the articulated spine of a child.

Several small fragments of bone were exposed during the 2017 excavation but due to their poor state of preservation, it was decided to plaster the whole feature and transport it for careful laboratory excavation. The plastered remains were first taken to the National Museums of Kenya (NMK), and then to the Conservation and Restoration laboratories at CENIEH in Burgos, Spain for mechanical and digital cleaning (Supplementary Information A).

Careful examination revealed the articulated partial skeleton of an immature human (Fig. 2). Sample OSL4, taken directly from the feature in 2013, was processed at Royal Holloway, London, resulting in a stratigraphically coherent age of 76.0 ± 7.4 ka (luminescence ages are presented at the 68.2% confidence interval throughout). Incorporation of this age into the Bayesian model yielded an estimated age of 78.3 ± 4.1 ka for the pit infilling (Extended Data Fig. 2, Supplementary Information C). Excavation of the sediment block encasing the skeletal elements revealed the presence of lithics and fauna (Supplementary Information B, Extended Data Fig. 1, Extended Data Table 1) that were consistent with the surrounding MSA layers. Layers 17-19 produced a large MSA lithic assemblage (n=2180) distinctive from the LSA layers above[8] and consistent with other MSA assemblages in eastern Africa[12]. Screening of the sediment and skeletal elements for ancient DNA proved inconclusive (Supplementary Information D).

Primary and intentional deposit

The hominin remains consist of a considerable part of the basicranium, a fragment of the left hemi-mandible with a complete ramus, five teeth (right M_1, right M^1, left dm^2 and the *in-situ* and un-erupted left M_1 and left M^1), the cervical and thoracic spine with associated ribs, the right clavicle, and the left humerus (Fig. 2 and Fig. 3). In addition, there were several fragments corresponding to the cranial, facial, pectoral, pelvic and limb areas, although anatomical identification is difficult due to postdepositional alteration (bioerosion, recrystallisation) of the bones (Extended Data Table 1, Supplementary Information E). Fragments of the left radius and ulna (in anatomical connection through a lump of sediment), and a deformed fragment of the left parietal, were also recovered, although detached from the main block. Several

unidentifiable bone fragments recovered in the field, prior to plastering the feature, probably correspond to the crushed and severely distorted upper part of the cranial vault. The advanced postdepositional alteration of the bones prevented the preservation and/or physical recovery of the remaining skeletal elements. Photographs taken after micromorphology sampling in 2013 show the proximal portion of the right femora inside the section (Supplementary Information A, Fig. 2) and photographs of the plan view in 2017 show the proximal end of the left femur (Fig. 1 b). Based on dental development we estimate that the child, which we named 'Mtoto' ('child' in Swahili), died at the age of 2.5-3.0 years (Supplementary Information F).

Four features[13], demonstrate that a fresh body was placed in a location where the entire process of decomposition took place: a) the macroscopic anatomical integrity of the body, especially unstable articulations; b) the minimal displacement of bones, with movements explained as a consequence of decompostition; c) the abundance of terrestrial gastropods that feed on earthworms in close proximity to the corpse; d) geochemical and histological analyses that indicate *in-situ* decomposition and putrefaction processes. All four criteria are met with the PYS child remains.

The majority of the bones appear in either strict articulation or good anatomical association and minor displacements can be explained as a consequence of decomposition and subsequent formation of secondary spaces. The combination of the photographic, surface scanner and microtomographic data, together with the total station coordinates of the pit feature, confirm that the body was deposited in a flexed right lateral decubitus position with the thighs flexed towards the torso at an angle less than 90º (Fig. 3, Extended Data Fig. 3). The vertebral column forms an arc stretching from the cervical to the distal thoracic area. This, together with the relative position of the lower limbs, denotes a tightly flexed position of the body. The body is

not lying flat, but the spine it is at an angle of approximately 12º above the horizontal axis. The thorax is laterally compressed. The ribs on the right side are flattened and those on the left side are at a higher angulation. There is a gap between the anterior ends of the right and the left ribs from the same vertebral level, consistent with the interpretation that the child's body was originally lying on its right side. Although the mechanical pressure of the sediment flattened the thorax, the rib cage did not collapse, preserving the original spatial relationship and curvature of the ribs, pointing to decomposition in a filled space. The preservation of most of the thorax articulations and thorax volume indicates that the destruction of the soft tissues and viscera did not produce a large, temporary empty space. This phenomenon tends to occur in contexts characterised by particularly fluid sediments that infiltrate by percolation and it is indirect but solid evidence of a deposit made in bare earth[13]. The particle size analysis confirms that the sediment inside the burial presents a higher proportion of both silt and sand and a lower proportion of clay in comparison to Layers 17-19 (except for two samples from top of Layer 18; Extended Data Fig. 4 and Supplementary Information G). This would favour a progressive infilling of the internal space as the cadaver decomposed and reinforces the hypothesis of an *in-situ* decomposition of the cadaver.

The right clavicle displays an oblique orientation, with a descent of the sternal extremity of almost 90º. Similarly, the first and second right ribs are also distally displaced, and rotated medially about 90º, but they preserve the intercostal space, arguing in favour of a minimal displacement of the sternal articulation of the pectoral girdle. The depression of the clavicle and the adoption of an oblique orientation are typical of tightly shrouded burial[14]. This is consistent with the upper part of the body being wrapped in a perishable cloth/material, or alternatively, the body being densely

packed within its pit structure. In either case, such a deliberate treatment of the body would explain the exceptional in-place preservation of the scapula and humerus of the over-hanging arm, and the intact articulation of the vertebral column and ribs, which would otherwise likely collapse as the decomposition advances[13].

Rotation of the head is common in burials as the result of gravity and decay, where the weight of the cranium shifts away from the cranio-vertebral attachments, placing it in an unstable position. For Mtoto, the cranium and the first three cervical vertebrae are disarticulated as a unit and partially dislocated from the column. The movement of the head points to the existence of some empty space around it and contrasts with the progressive infilling and minimal displacement of the rest of the body. In a fresh cadaver, this type of head dislocation involving the cervical vertebrae could indicate collapse due to the decay of a perishable support placed beneath the head[15,16]. Mtoto's head dislocation, together with the depression of the clavicle and the first two ribs, is compatible with the upper part of the body being wrapped and the head supported with a perishable material. The differential preservation of the upper versus the lower part of the body could be additional evidence for this protective treatment. This evidence is supportive of a more elaborated involvement of the community in the funerary rite versus structured abandonment of a corpse[5] or a happenstance burial[17].

The anatomical integrity and strict articulation of some unstable articulations indicate a primary and undisturbed deposit[13,14] and that the child was covered with sediment rapidly after its placement. Taphonomical, histological and geochemical analyses support the *in-situ* decomposition and putrefaction. The anatomical alignment and advanced diagenesis of Mtoto contrasts with the highly fragmented status and more variable diagenetic conditions of faunal remains from Layers 17-19

(Extended Data Table 1, Supplementary Information H). All available evidence argues in favour of rapid burial after death, protecting the skeleton from intense post-depositional breakage as experienced by the faunal remains in the surrounding layers.

Optical microscopy of Mtoto's upper limb bone fragments demonstrates that human and non-human bone followed different taphonomic trajectories. The most parsimonious interpretation of the bioerosion, recystallisation, and Fe oxide deposition pattern on the human bone, and of the micromorphological characteristcis of the burial sediment matrix, is that the child's body decomposed as a buried fleshed cadaver, in an episodically waterlogged burial environment (Supplementary Information E). The skull presents several star-shaped marks and bore holes indicative of insect and gastropod activity, compatible with *in-situ* decomposition (see [18] and Supplementary Information H Fig. 2).

Higher concentrations of MnO and CaO in the pit fill are also consistent with *in-situ* decomposition of the body and mediated by putrefactive bacteria[19,20]. (Supplementary Information E and Extended Data Figs. 5-6, Extended Data Table 2).

The sediment matrix is devoid of microcharcoal, ash or other microscopic (putative) human inputs. Five land snail shell fragments (*Achatina* sp.) were found in close association with the skeleton, around the occipital area. One of these shell fragments bear lines incised by a point, not seen in fragments from the encasing layers (Extended Data Fig. 7, Supplementary Information I). *Achatina* sp. fragments, however, are also abundant in penecontemporaneous Layer 18 and bear traces of heating and consumption. Thus, the evidence is not sufficient to suggest deliberate placement of shell fragments in the pit. Nevertheless, the *Achatina* shells from the pit are significantly larger in comparison to those from penecontemporaneous Layer 18, indicating that they did not experience intensive breakage from processes such as

trampling (Supplementary Information I). Analysis of reddish agglomerates spotted during the excavation of the child's remains showed that they were not anthropogenic in origin.

Burial versus funerary caching

In addition to the primary placement of the body, the recognition of a burial requires the identification of a purposedly excavated pit followed by intentional covering of the corpse[5]. The distinction of a new stratum is key to distinguishing a burial from the accommodation of a body in natural places such as cave fissures or hollows, a practice known as funerary caching[5,21]. The PYS stratigraphy provides evidence in favour of an intentional burial. The excavation of Trench 4 exposed a distinct feature, a demarcated pit with sediment matrix that differed in colour and texture from the remainder of the sequence, and which can only have resulted from intentional digging into Layer 19. The burial fill is a mix of ferruginous silt and sand, compositionally similar to the top of Layer 18 and the base of Layer 17, and different from Layer 19 in which the pit was excavated (Extended Data Fig. 4, Supplementary Information G). The fine-grained texture of the intraskeletal matrix may be representative of the original composition of the burying sediment or it may have resulted from infiltration of the sediment between the bones as the cadaver skeletonised (Supplementary Information E and Extended Data Figs. 5-6, Extended Data Table 2). This is compatible with the evidence of a progressive infilling in a deposit made in bare earth. The lack of diagnostic features of flood and/or mass flow in the burying sediment makes it unlikely that the sediment was washed into the pit during a flood event shortly after the deposition of the corpse. The most parsimonious

interpretation is that Mtoto's body was deliberately covered using backfill sediment scooped from the colluvial deposits that made up the Layer 18 cave floor.

In sum, the interpretation for an intentional burial[5,17] of Mtoto is based on: a) the identification of a clear pit feature dug into Layer 19; b) the geochemical and granulometric evidence discriminating the burial fill from the surrounding layers, suggesting that sediment gradually filtered in empty spaces created by the decomposition of the body and insect activity; c) the overall completeness and anatomical integrity of the skeleton and the alignment of the body in a tightly flexed position in the pit consistent with a rapid covering after the body's deposition; and, d) the striking difference between the unique depositionary and taphonomic history of the child remains and that of the faunal assemblage from the same layers.

Taxonomic assessment

Mtoto's teeth were compared against a large dental sample representative of *H. neanderthalensis* and recent and fossil *H. sapiens*. Several crenulations and mesial accessory tubercles make the PYS dm^2 more primitive than recent counterparts (Extended Data Fig. 8 and Supplementary Information F). The PYS M^1 samples fall within the range of variation of *H. sapiens*, although it resembles the morphologically more complex Aterian individuals in its pronounced Carabelli expression and the exceptionally large and subdivided hypocones[22]. In both the dm^2 and the M^1, the occlusal polygon is more rhomboidal than in fossil and recent *H. sapiens*, but not as skewed as in Neanderthals. The size cusp sequence of the M^1 falls between recent and Upper Palaeolithic *H. sapiens* on the one hand, and Neanderthals and Qafzeh on the other. Although the M_1 morphology is compatible with that of *H. sapiens*, the profuse crenulation of their enamel makes these more complex than those of recent modern

304 humans and some fossil *H. sapiens* from Africa, the Levant, Europe and East
305 Asia[23,24]. The size cusp sequences in the M_1s are intermediate between that found in
306 early *H. sapiens* specimens and in Neanderthals and recent *H. sapiens*[25]. The shape
307 analysis of the occlusal outline of the EDJ reveals that all PYS teeth cluster with
308 modern humans except for the M_1 that is closer to Neanderthals (Extended Data Fig.
309 8). The dimensions of Mtoto's teeth fall within the range of variation of recent
310 modern humans. The enamel of both deciduous and permanent molars of PYS is thick
311 – a primitive condition shared with *H. sapiens* and the majority of speciments in the
312 hominin fossil record except for Neanderthals (Supplementary Information F Fig. 1).
313 Mtoto's dentition is consistent with an assignment to *H. sapiens,* although it
314 preserves some primitive features indicating that the child was morphologically less
315 derived than other broadly contemporaneous populations. The mandibular ramus
316 shows a symmetric mandibular notch, where the condylar and coronoid processes are
317 levelled. This, together with the strongly arched temporal squama, align Mtoto with
318 modern humans.
319
320 **Implications of the PYS burial for human cultural evolution**
321
322 Despite Africa's alleged centrality for the emergence of 'modern human
323 behaviour' in the late Middle Pleistocene[1,26], early evidence for morturay practices in
324 the continent is scarce. Until now, the two earliest possible burials in Africa were that
325 of Taramsa, Egypt, and Border Cave, South Africa. At Taramsa, a skeleton of a child,
326 dated to 68.6 ± 8 ka, was recovered in a pit similar to nearby MSA chert extraction
327 pits[27–29]. Since the pits relate to chert mining, Taramsa is interpreted as a late example
328 of a long-lasting caching tradition in *H. sapiens*[5]. The infant hominin (BC3) found in

329 1941 at Border Cave, thought to date to ~74 ± 4 ka[30], was apparently associated with a
330 single perforated and ochred *Conus* shell. Although recent reapprisal of the evidence
331 confirms the presence of a pit, documentation on this burial is unfortunately limited.
332 No information is available on the degree of articulation and the position of the
333 remains[31,32] within the pit, and its age is inferred from a stratigraphic correlation with
334 an ESR-dated section, located more than 10 m away from the pit. Although the
335 chronological and stratigraphic data for BC3 is consistent with an age not younger
336 than 58 ka[30], and possibly as old as 74 ka, a more constrained chronology for the
337 skeleton is not available.

338 The contextual, chronological and taphonomic information available at PYS
339 are supportive of a primary burial and meet the criteria for simple, early inhumations
340 of hominins in the Late Pleistocene[5]. On the basis of multiple, and stratigraphically
341 coherent OSL dates, PYS represents the earliest evidence of an intentional burial in
342 Africa at 78.3 ± 4.1 ka, clearly demonstrating that complex treatment of the dead was
343 practiced by *H. sapiens* by late MIS 5. The PYS burial reveals a clear and direct
344 association between *H. sapiens* and MSA technology. This association is relevant in
345 the light of current scenarios on the emergence of our species[2,3], which emphasize the
346 joint role of different African populations in this process and the possibility of
347 regional asynchronicity in the emergence of key modern anatomical and cultural
348 traits.

349 The PYS child, in combination with the infant burial from Border Cave and
350 the funerary caching of a juvenile at Taramsa[5], suggests that *H. sapiens* populations
351 were intentionally preserving the corpses of young members of their groups between
352 ~78-69 ka. Prior to 78 ka, there are no unambiguous burials of modern humans in
353 Africa, despite the fact that earlier MSA populations demonstrate sophisticated forms

of symbolic expression[33–36]. Before that, intentional defleshing has been inferred on the 600,000 year-old Bodo cranium[37], and the juvenile specimen from Herto[38]. Funerary caching has been proposed for the Atapuerca-Sima de los Huesos hominins (Spain)[4,5] and *H. naledi* (South Africa)[39].

The African evidence provides a point of contrast with Neanderthals and early modern human mortuary behaviours in Eurasia. Neanderthals and modern humans commonly buried their dead in residential sites from at least ~120 ka[40]. Infant and child burials are ubiquitous in Neanderthal and early modern human sites in the Levant and Europe, comprising 55-35% of all known Middle Palaeolithic and MSA interments after 120 ka[40]. Burial in residential localities, such as at PYS, has been suggested to reflect mourning behaviour and the intention to keep the dead nearby[40]. Despite being the cradle of *H. sapiens*[41], Africa demonstrates a scarcity of mortuary practices over most of the MSA that provides little current support for modern-like conceptions of the afterlife and/or treatment of the dead. Nonetheless, cross-cultural evidence in *H. sapiens* clearly emphasises that the absence of a behaviour does not necessarily imply that capacity for such behaviour was lacking. Evidence for advanced planning and symbolism is present by ~320 ka, and particularly after 100 ka in eastern Africa and southern Africa[42–44]. The absence of burials from the onset of the MSA by ~320ka[45] and the rare occurrence of burials after 78 ka, may be due to a variety of factors, including cultural practices that leave elusive archaeological traces or a shift, sometime between 150 ka and 80 ka, from defleshing and curation[38] to funerary caching and burials, observed at more recent sites from eastern Africa. The PYS burial shows that inhumation of the dead is a practice shared by populations living inside and outside Africa during the last interglacial.

The ~78.3 ka-old PYS skeletal remains are of interest for the insight they provide about the evolution of our species in Africa. While the mandibular and dental assessment of Mtoto are consistent with its assignment to *H. sapiens*, the preservation of some primitive dental features in comparison to other penecontemporaneous populations suggests that our species may have evolved in subdivided and regionally distinct populations and in a variety of paleocological settings (Supplementary Information J). Our study reaffirms the suggestion that the biological and socio-cultural evolution of *H. sapiens* was a complex and regionally diverse process.

References

1. McBrearty, S. & Brooks, A. S. The revolution that wasn't: a new interpretation of the origin of modern human behavior. *J. Hum. Evol.* **39**, 453–563 (2000).
2. Mounier, A. & Lahr, M. M. Deciphering African late Middle Pleistocene hominin diversity and the origin of our species. *Nat. Commun.* **10**, 3406 (2019).
3. Scerri, E. M. L. *et al.* Did our species evolve in subdivided populations across Africa, and why does it matter? *Trends Ecol. Evol.* **33**, 582–594 (2018).
4. Carbonell, E. & Mosquera, M. The emergence of a symbolic behaviour: the sepulchral pit of Sima de los Huesos, Sierra de Atapuerca, Burgos, Spain. *C. R. Palevol* **5**, 155–160 (2006).
5. Pettitt, P. *The Palaeolithic Origins of Human Burial*. (Routledge, 2011).
6. Zilhão, J. Lower and Middle Palaeolithic mortuary behaviours and the origins of ritual burials. in *Death Rituals and Social Order in the Ancient World: Death Shall Have No Dominion* (eds. Renfrew, C., Boyd, M. J. & Morley, I.) 27–44 (Cambridge University Press, 2016).

7. Roberts, P. *et al.* Late Pleistocene to Holocene human palaeoecology in the tropical environments of coastal eastern Africa. *Palaeogeogr. Palaeoclimatol. Palaeoecol.* **537**, 109438 (2020).
8. Shipton, C. *et al.* 78,000-year-old record of Middle and Later Stone Age innovation in an East African tropical forest. *Nat. Commun.* **9**, 1832 (2018).
9. d'Errico, F. *et al.* Trajectories of cultural innovation from the Middle to Later Stone Age in eastern Africa: personal ornaments, bone artifacts, and ocher from Panga Ya Saidi, Kenya. *J. Hum. Evol.* **141**, 102737 (2020).
10. Prendergast, M. E. *et al.* Reconstructing Asian faunal introductions to eastern Africa from multi-proxy biomolecular and archaeological datasets. *PLoS ONE* **12**, e0182565 (2017).
11. Skoglund, P. *et al.* Reconstructing prehistoric African population structure. *Cell* **171**, 59-71.e21 (2017).
12. Grove, M. & Blinkhorn, J. Neural networks differentiate between Middle and Later Stone Age lithic assemblages in eastern Africa. *PLoS ONE* **15**, e0237528 (2020).
13. Duday, A. L'archéothanatologie ou l'archaéologie de la mort. in *Social Archaeology of Funerary Remains* (eds. Gowland, R. L. & Knüsel, C. J.) 30–56 (Oxbow Books, 2006).
14. Knüsel, C. J. Crouching in fear: terms of engagement for funerary remains. *J. Soc. Archaeol.* **14**, 26–58 (2014).
15. Blaizot, F. Les espaces funéraires de l'habitat groupé des Ruelles à Serris du VIIe au XIe siècles Seine et Marne, I^le-de-France: taphonomie du squelette, modes d'inhumation, organisation et dynamique. (Université de Bordeaux, 2011).

16. Kapandii, I. A. *Physiologie Articulaire: Schémas Comment Mécanique Humaine*. vol. 3: Tronc et Rachis (Maloine, 1972).
17. Defleur, A. *Les Sépultures Moustériennes*. (Editions de CNRS, 1993).
18. Backwell, L., Huchet, J.-B., Jashashvili, T., Dirks, P. H. G. M. & Berger, L. R. Termites and necrophagous insects associated with early Pleistocene (Gelasian) Australopithecus sediba at Malapa, South Africa. *Palaeogeogr. Palaeoclimatol. Palaeoecol.* **560**, 109989 (2020).
19. Ghiorse, W. C. The biology of manganese transforming microorganisms in soil. in *Manganese in Soils and Plants* (eds. Graham, R. D., Hannam, R. J. & Uren, N. C.) 75–85 (Springer Netherlands, 1988).
20. Thompson, I. A., Huber, D. M., Guest, C. A. & Schulze, D. G. Fungal manganese oxidation in a reduced soil. *Environ. Microbiol.* **7**, 1480–1487 (2005).
21. Gargett, R. H. Middle Palaeolithic burial is not a dead issue: the view from Qafzeh, Saint-Césaire, Kebara, Amud, and Dederiyeh. *J. Hum. Evol.* **37**, 27–90 (1999).
22. Bailey, S. E. & Hublin, J.-J. Did Neanderthals make the Châtelperronian assemblage from La Grotte du Renne (Arcy-sur-Cure, France)? in *Neanderthals Revisited: New Approaches and Perspectives* (eds. Hublin, J.-J., Havarti, K. & Harrison, T.) 191–209 (Springer, 2006).
23. Grine, F. E. Middle Stone Age human fossils from Die Kelders Cave 1, Western Cape Province, South Africa. *J. Hum. Evol.* **38**, 129–145 (2000).
24. Liu, W. *et al.* The earliest unequivocally modern humans in southern China. *Nature* **526**, 696–699 (2015).

25. Martín-Albaladejo, M., Martinón-Torres, M., García-González, R., Arsuaga, J. L. & Bermúdez de Castro, J. M. Morphometric analysis of Atapuerca-Sima de los Huesos lower first molars. *Quat. Int.* **433**, 156–162 (2017).
26. Henshilwood, C. & Marean, C. W. The origin of modern human behavior: critique of the models and their test implications. *Curr. Anthropol.* **44**, 627–651 (2003).
27. Janssen, J., Gijselings, G., Paulissen, E. & Vermeersch, P. M. Middle Palaeolithic chert exploitation pits near Qena (Upper Egypt). *Paléorient* **12**, 61–65 (1986).
28. Van Peer, P., Vermeersch, P. M. & Paulissen, E. *Chert Quarrying, Lithic Technology and Human Burial at the Palaeolithic Site of Taramsa 1, Upper Egypt*. vol. 5 (Leuven University Press, 2010).
29. Vermeersch, P. M. *et al.* A Middle Palaeolithic burial of a modern human at Taramsa Hill, Egypt. *Antiquity* **72**, 475–484 (1998).
30. d'Errico, F. & Backwell, L. Earliest evidence of personal ornaments associated with burial: the conus shells from Border Cave. *J. Hum. Evol.* **93**, 91–108 (2016).
31. Beaumont, P. B., de Villiers, H. & Vogel, J. C. Modern man in sub-Saharan Africa prior to 49000 years BP: a review and evaluation with particular reference to Border Cave. *S. Afr. J. Sci.* 409–419 (1978).
32. Cooke, H. B. S., Malan, B. D. & Wells, L. H. Fossil man in the Lebombo Mountains, South Africa: the 'Border Cave,' Ingwavuma District, Zululand. *Man* **45**, 6–13 (1945).

33. d'Errico, F. *et al.* Additional evidence on the use of personal ornaments in the Middle Paleolithic of North Africa. *Proc. Natl. Acad. Sci.* **106**, 16051–16056 (2009).
34. Henshilwood, C., d'Errico, F. & Watts, I. Engraved ochres from the Middle Stone Age levels at Blombos Cave, South Africa. *J. Hum. Evol.* **57**, 27–47 (2009).
35. Henshilwood, C. S. *et al.* An abstract drawing from the 73,000-year-old levels at Blombos Cave, South Africa. *Nature* **562**, 115–118 (2018).
36. Steele, T. E., Alvarez-Fernandez, E. & Hallet-Desguez, E. Personal ornaments in early prehistory: a review of shells as personal ornamentation during the African Middle Stone Age. *Paleoanthropol.* **24**, 24–51 (2019).
37. White, T. D. Cut marks on the Bodo cranium: a case of prehistoric defleshing. *Am. J. Phys. Anthropol.* **69**, 503–509 (1986).
38. Clark, J. D. *et al.* Stratigraphic, chronological and behavioural contexts of Pleistocene Homo sapiens from Middle Awash, Ethiopia. *Nature* **423**, 747–752 (2003).
39. Dirks, P. H. G. M. *et al.* Geological and taphonomic evidence for deliberate body disposal by the primitive hominin species Homo naledi from the Dinaledi Chamber. *Elife* **4**, e09561 (2015).
40. Stiner, M. C. Love and death in the Stone Age: what constitutes first evidence of mortuary treatment of the human body? *Biol. Theory* **12**, 248–261 (2017).
41. Scerri, E. M. L., Chikhi, L. & Thomas, M. G. Beyond multiregional and simple Out-of-Africa models of human evolution. *Nat. Ecol. Evol.* **3**, 1370–1372 (2019).

42. Brooks, A. S. *et al.* Long-distance stone transport and pigment use in the earliest Middle Stone Age. *Science* **360**, 90–94 (2018).
43. Henshilwood, C. S. *et al.* A 100,000-year-old ochre-processing workshop at Blombos Cave, South Africa. *Science* **334**, 219–222 (2011).
44. Wadley, L. Theoretical frameworks for understanding African hunter-gatherers. in *The Oxford Handbook of African Archaeology* (eds. Mitchell, P. & Lane, P.) 15 (Oxford University Press, 2020).
45. Richter, D. *et al.* The age of the hominin fossils from Jebel Irhoud, Morocco, and the origins of the Middle Stone Age. *Nature* **546**, 293–296 (2017).

Fig. 1: Location of PYS and stratigraphic context of burial. **a**, PYS is located in the uplands of Kenya's coastal plain. Panel on right side shows the 19 stratigraphic layers with the location of burial pit at bottom of MSA Layer 18 and in Layer 19. Detailed inset of burial pit shows piece-plotted objects, including MSA lithics and fauna and three associated OSL dates in Layers 17-19. The Bayesian age is 78.3 ± 4.1 ka. **b**, Plan view of the 2017 excavation. The black line delimits the pit feature and the change in texture from the surrounding matrix. The faint white outline of the decomposed skull, spine, femur and other severely degraded bones can be observed on the surface of the pit. **c**, Same view with the superimposition of the virtual reconstruction of the CT and surface scans of Mtoto. The preserved parts (solid) are superimposed over a semi-transparent comparative skeleton to better depict the position of the child.

Fig. 2: PYS human fossil. **a**, External view of the PYS main block where the flexed spine with articulated vertebrae and ribs, as well as some teeth are partially exposed on the surface. The photograph was taken after the initial cleaning and removal of

three right thoracic ribs, which revealed how the first and second ribs descended and rotated into the thoracic cavity while preserving the intercostal space. This argues in favour of minimal displacement of this part of the body as a unit given the sternal articulation of the pectoral girdle. **b**, External view of the left side of Mtoto's skull and left hemimandible showing the strict and intact temporo-mandibular articulation. The photograph was taken after the skull was cleaned and separated from the postcranial elements. The unerupted M_1 and M^1 are held in place despite the fact that their roots were not developed, supporting the interpretation of an undisturbed deposit. The first three cervical vertebrae are rotated but in place, and connected to the foramen magnum.

Fig. 3: Mtoto's preservation and position in the pit. a, Preserved parts of the PYS skeleton. Front **b** and top **c** view of the virtual reconstruction of the preserved skeletal parts (solid) superimposed over a transparent comparative skeleton. The fragments of both the left and right femora could not be recovered, but their outline was identified on the plan view and in the wall profile, marked as a solid line over the transparent skeleton. The position of the right radius and ulna fragments and the right parietal are approximate, since they were found detached from the original block.

Methods

Luminescence dating

A suite of seven quartz single-grain optically stimulated luminescence (OSL) ages for PYS were previously published, including a detailed description of the luminescence measurement and data analysis techniques used (their Supplemental Note 3 Shipton et al. 2018[8]). These data were stratigraphically consistent, and were combined with a

number of radiocarbon ages to construct an age model using Bayesian software (OxCal 4.4.2). The resulting chronology was internally consistent, but analysis of the single-grain data from samples located towards the base of the sedimentary sequence indicated that a high proportion of the grains were close to "saturation" i.e. they had received a natural radiation dose which was sufficiently close to the saturation dose to preclude the calculation of an accurate De value. Both the method used to identify saturated quartz grains[46], and the presence of a high proportion of such grains[47], have the potential to cause age underestimates. Consequently, in the present study single-grains of potassium feldspars (K-feldspar) from five samples from PYS were measured using a post-infrared, infrared stimulated luminescence (pIRIR) measurement protocol[48]. These measurements were performed on the two deepest (oldest) previously published samples (PYS13-OSL3 and OSL5), a new sample from the burial (PYS13-OSL4), and two younger samples (PYS13-OSL11 and OSL17). Since K-feldspar is known to saturate at much higher doses than quartz, this approach allows the accuracy of the older published ages to be tested. Measurement and data analysis procedures are described in Supplementary Information C.

The K-feldspar measurements, combined with reanalysis of the quartz data, indicate that the published OSL ages[8] for Layers 17 and 18 are underestimates, but those for younger layers are accurate. Ages deemed to be accurate were incorporated into a new age model using Bayesian software (OxCal 4.4.2). The K-feldspar age for the PYS13-OSL4, the sample within the burial, is consistent with those for the surrounding sediments (PYS13-OSL3 and OSL5). If the burial pit had been dug into much older sediments and then infilled using those sediments, some grains would probably have had their luminescence signal reset during the process. This might be expected to yield a younger age for the burial infill than the surrounding sediments,

572 which is not the case for the K-feldspar ages. The quartz ages for these samples,
573 although believed to be underestimates, are also indistinguishable. Also, the
574 overdispersion of the quartz data is similar for samples PYS13-OSL3-5. This suggests
575 the burial occurred sufficiently shortly after deposition of layers 17 and 18 that
576 bleaching of grains during the excavation and infilling processes did not increase the
577 scatter of equivalent doses. The similarity in K-feldspar ages and quartz
578 overdispersion between samples PYS13-OSL3-5 does not unequivocally demonstrate
579 that the burial infill is contemporaneous with Layers 17 and 18, since if the pit was
580 backfilled with spoil this might have occurred under subdued light conditions leading
581 to poor luminescence signal resetting. Also, given the ~7-10% uncertainties on
582 individual K-feldspar ages, archaeologically important differences in age could go
583 unnoticed. Nonetheless, the absence of a discrepancy between the ages and
584 overdispersion of the burial infill and surrounding sediments suggests that the burial
585 is contemporaneous with Layers 17/18, at least at the temporal resolution achievable
586 using luminescence techniques.

587 **Bayesian Modelling and age of the PYS burial**

588 Bayesian modelling enables the relative stratigraphic information recorded during
589 excavation to be formally incorporated into posterior age estimates deriving from
590 chronometric data expressed as probability distributions (in this case calibrated
591 radiocarbon and luminescence probability distributions) and 'prior' information, i.e.
592 observations on the data we collect. In archaeology, this is often the stratigraphic and
593 other relative information. Hence 'posterior' data, is a probability function that
594 reflects the level of confidence associated with the values of the unknown parameters,
595 in this case chronometric measurements, after the observation of the prior

information. Details about the data and structure of comprehensive model for the dating of the PYS sequence were described previously[7].

Here we update the model, using recalculated OSL ages for Layers 9-15, replacing OSL ages for Layers 17 and 18 with new PIRIR ages and adding the new pIRIR age obtained for the burial infill (OSL4). The standard errors associated with the luminescence ages include both the random and systematic uncertainties. This updated model was run using OxCal 4.4.2[49], and the code is shown in Supplementary Information C. By inserting a "Date" command in the OxCal structure we allow the model to find the best fit for the age of the burial based on all luminescence ages obtained for relevant Layers 17 and 18 (Supplementary Information C Table 4). Because of uncertainties in the bleaching history of sediment grains deriving from disturbed contexts, such as a burial, we do not tie the "Date" command to OSL4; instead we treat the burial infill sediment as another independent age for Layer 18.

Given that Layers 17 and 18 are statistically indistinguishable from each other and from OSL4, we may assume that both layers are quasi-contemporaneous, at least in the precision offered by the luminescence methods, for the studied period. The new model is shown in Extended Data Figure 1.

Screening for Ancient DNA

DNA extraction and library preparation. We screened for ancient DNA 8 undiagnosed skeletal fragments and 12 sediment samples associated with the PYS burial pit (Supplementary Information D Table 1). DNA was extracted from ~50mg of bone or sediment using a silica-based method developed for the retrieval of short DNA molecules[50] on an automated liquid handling platform[51]. 15% of each extract

were converted into a single-stranded DNA library[52], and barcoded with a pair of unique indices[53], following the modifications described in Korlević et al. (2015)[54]. The number of DNA molecules incorporated into each library was assessed by quantitative PCR as described elsewhere[55]. Extraction and library negative controls were carried through all steps of the experiments. Libraries were pooled and shotgun sequenced on a HiSeq platform (Illumina).

Mitochondrial capture and sequencing. 1 µg of each amplified DNA library was enriched whether for mammalian mitochondrial DNA (mtDNA) using a probe set of 242 taxa[56] or for human mtDNA with a probe set covering the full human mitochondrial genome[57,58]. The enriched libraries were pooled in two sets according to the capture probe used and sequenced on a MiSeq platform (Illumina).

Sequence processing and mapping. The reads obtained from the sequencing of the mtDNA enriched libraries were trimmed to remove adapter sequences and overlapping paired-end reads were merged using leeHom[59]. Sequences from the mammalian mtDNA enriched libraries were aligned to a non-redundant database of 796 mammalian mitochondrial genomes from the NCBI Reference Sequence database (RefSeq) using nucleotide BLAST (BlastN)[60] with default parameters. Sequences were then assigned to different taxa using MEGAN[61] and each ancient taxon is deemed present in the dataset according to the requirement described earlier[62]. The sequences from the human mtDNA enriched libraries were aligned to the revised Cambridge Reference mitochondrial genome (rCRS, NC_0120920) using the Burrows-Wheeler Aligner (BWA)[63] with optimized parameters for ancient DNA «-n 0.01 –o 2 –l 16500»[64]. Aligned sequences shorter than 35 bases with a mapping

quality lower than 25 were filtered out. PCR duplicates were removed by merging sequences with identical alignment start and end coordinates using bam-rmdup (https://github.com/mpieva/biohazard-tools).

Virtual reconstruction

PYS was recovered encased in a block and had to be manually and mechanically prepared for study. Given the delicate preservation and the infantile age stage of the specimen, a microCT scan was performed to extract digital 3D models of the teeth and bones, which were still embedded within the sediment. Because of the delicate state of preservation and the need of preserving the information regarding the position of the body a combination of mechanical and virtual isolation of the skeleton was decided. However, the low density of the bones prevented a proper virtual isolation of the elements, and it was necessary to carefully isolate the cranial from the postcranial elements (Supplementary Information A) and to combine microCT and surface scanners to reconstruct the original position of the child inside the block. The microCT scans were performed at the Laboratory of Microscopy of the Centro Nacional de Investigacion sobre la Evolucion Humana–Unique Scientific & Technical Infrastuctures (CENIEH–ICTS, Burgos, Spain) with a Phoenix v|tome|x s (GE Measurement & Control). First, the entire block was scanned at 140 kV and 400 μA, with a 0.2 mm Cu filter and an integration time of 333 ms, resulting in an isometric voxel size of 0.1227 mm. As the remains were carefully manually cleaned, we performed a microCT of the block containing the cranial remains at 200 Kv and 400 μA, with the same filter and integration time, resulting in an isometric voxel size of 0.0769 mm, and another scan of the block containing the postcranial elements at 140kV and 250 μA, with the same filter and integration time, resulting in an isometric

669 voxel size of 0.0479 mm. Each isolated tooth as well each smaller block resulting
670 from the mechanical excavation were also microCT scanned. Additionally, surface
671 scanners with a hand scanner (Artec Space Spider) under conditions of artificial light
672 were performed of each excavated element and processed with Artec Studio 11
673 software to create surface models. Digital cleaning and segmentation were performed
674 with Mimics 18.0 (Materialise, Be) and Avizo 7.0 (Visualization Sciences Group,
675 2012) using a combination of automatic and manual segmentation, generating STL
676 files of all PYS remains. Digital renderings of the specimen in several views were
677 done with Avizo, Mimics and MeshLab, respectively. With the digital renders, it was
678 possible to identify several anatomical elements, such as the first vertebrae in
679 anatomical connection. The identification of two teeth and several shells in the first
680 microCT of the main block was useful as reference landmarks to later orient the
681 microCT of the skull and the CT and surface scanner of the thorax in their original
682 position. Furthermore, and to understand the position of the child within the block, the
683 skull of a *Homo sapiens* child in a similar stage of development was microCT
684 scanned and virtually reconstructed. Using Mimics and MeshLab software, both PYS
685 and *Homo sapiens* crania were superimposed with the registration and align tool. A
686 best-fit was made to reference them in the best position and see which parts were
687 deformed or displaced. Furthermore, both crania were placed again in the burial pit
688 using as a reference the 2 teeth identified in the first microCT scan of the main block.
689 In addition, a comparative human skeleton of *H. sapiens* of similar age was scanned
690 using the same surface scanner to obtain the digital models of all the long bones, hips
691 and ribs, to help reconstruct the original position of the child inside the burial. Using
692 Mimics software, all the models were scaled to obtain a length similar to that of a 2.5-
693 3 year old (following Scheuer and Black, 2000[65]). To align the comparative skeleton

694 with the PYS remains, the STL models of the vertebral column, ribs, clavicle, scapula
695 and humerus were aligned using both the CT of the entire block and the CT of the
696 PYS vertebral column.
697 Once all the remains and comparative models were aligned, 3ds Max 2020
698 (Autodesk) was employed combing the topopgraphic information available from the
699 field, photographs of the excavation plan, all the STL and OBJ models of both Mtoto
700 and the comparative skeleton to produce the closest reconstruction of the original
701 position of the child when it was found at the siate. Each anatomical element was
702 reoriented following the topographic field information and the orthophotos of the site.
703 When all the remains were located in space, we proceeded to create textures, shadows
704 and lights, to visualize the preserved skeletal elements and to integrate them in their
705 original position in the comparative skeleton. Some renderings have been made with
706 the semi-transparent comparative skeleton, to understand and visualize the position of
707 the PYS into the burial, and understand its anatomical connection.
708
709 **Thin section micromorphology and bone microscopy**
710 A micromorphology sample collected in a 6x10 cm polyurethane box at the end of the
711 2013 field season (PYS 2013_M1:19/18) intercepted soft, degraded bone. This
712 sample was not processed for micromorphological analysis: it was stored until 2019,
713 when it became apparent that it may have contained parts of Mtoto's skeleton
714 (probably fragments of lower limbs and ribs). The box was then excavated at
715 CENIEH (Burgos). In the course of this excavation, centimetre-sized bone fragments
716 and lumps of the sediment matrix were collected for microscopic investigation. Bone
717 and sediment were air dried and impregnated with polyester resin under desiccation
718 vacuum. One uncovered petrographic thin section (30µm thick) was produced from

719 the impregnated block. The section was examined under a polarizing microscope (x10
720 to x400) at plane polarized (PPL), cross-polarized (XPL) and oblique incident light
721 (OIL). Description of sediment features follows Bullock et al. (1985)[66], Stoops
722 (2003)[67] and Stoops et al. (2018)[68]. Estimates and measurements of sediment
723 inclusions and histological attributes of the bone fragments were made with the aid of
724 standard semi-quantitative estimation charts and the *analySIS pro5* image analysis
725 software. The degree of diagenetic alteration of bone was estimated mainly through
726 optical microscopy, using the General Histology Index (GH[69]) – an estimate of
727 microstructural alteration similar to the more commonly used Oxford Histology Index
728 (OHI[70,71]), but taking into account other types of structural and compositional
729 alteration (generalised destruction, staining, accumulation of authigenic deposits,
730 fissuring) besides bioerosion. Where identifiable, microscopic bioerosion
731 ("*microscopical focal destruction*" – MFD[72] was recorded following the typology
732 proposed by Hackett (1981)[72] and Jans (2008)[73]. SEM-EDS analysis (on a Zeiss
733 EVO-MA15, with an Oxford Instruments InCA Max 80 mm EDS) was carried out on
734 the polished, uncoated thin section, to observe bone microstructure at higher
735 magnifications and determine elemental composition of selected features. Low-
736 vacuum conditions were used (60 Pa) to prevent charging of the sample surface; strict
737 operating conditions of 50 μA filament current, 2.525 A gun current, 20 kV
738 accelerating voltage, and an 8.5 mm working distance to achieve an acquisition rate of
739 15 kcps, were applied to standardise the analyses. A polished Co standard was
740 analysed to adjust for beam current drift, and a polished dolomite standard was used
741 to confirm the accuracy of the calculated absolute element concentrations. Navigation
742 on the sample was aided by section scans. Data are reported as non-normalised
743 percentage weights.

744

745 **Dental analysis**

746

747 **Comparative metrical and morphological study of teeth**. The evaluation of
748 morphological features was made on the original fossils and the virtual images
749 obtained by microtomography. The descriptive terminology used in this report derives
750 from the following sources: Carlsen (1987)[74], Tobias (1991)[75], Turner et al. (1991)[76],
751 Scott and Turner (1997)[77], Martinón-Torres et al. (2007)[78], Martinón-Torres et al.
752 (2008)[79], Martínez de Pinillos et al. (2017)[80], and Table 4 in Martinón-Torres et al.
753 (2012)[81], which includes a modified version of the Arizona State University Dental
754 Anthropological System (ASUDAS) of scoring. Occlusal wear was recorded
755 following Molnar (1971)[82]. The comparison was focused in the Late Pleistocene
756 samples, *H. sapiens* and *H. neanderthalensis*, although several samples from the
757 Middle to late Pleistocene Africa were included in order to assess the variability of
758 the African fossil record. The mesiodistal (MD) and buccolingual (BL) dimensions of
759 the PYS child were measured by JMBC to the nearest 0.1 mm, following the methods
760 of Flechier, Lefêvre, and Verdéne (1973)[83]. Apart from the MD and the BL, we have
761 also calculated the computed crown area (CCA: MD X BL) and the measured crown
762 area (CI: [BL/MD] x 100). In addition, the cusp areas of the M1s were measured
763 following Bermúdez de Castro et al. (2001)[84] and using the criteria outlined by Bailey
764 (2004)[85]. The areas were measured three times and the average of the three values was
765 used. The total crown base area (TCBA) was calculated as the sum of all the
766 individual cusp areas. The PYS values were compared against a large hominin sample
767 of *H. sapiens, H. neanderthalensis* and some relevant Middle to Late Pleistocene
768 fossils from Africa.

769 **Enamel Thickness**. Virtual sectioning of the molars was performed following the
770 protocol described in Olejniczak and colleagues (2008)[86]. The mCT image stack was
771 imported into Amira (6.3.0, FEI Inc.) and rotated into anatomical position. Then, the
772 tip of three dentine horns (protoconid, metaconid and hypoconid in the mandibular
773 molars and protocone, paracone and hypocone in the maxillary molars) were
774 identified and the image stack was adjusted to intersect these three points of interest.
775 A new plane perpendicular to the plane containing the three dentine horns was rotated
776 to pass through the mesial dentine horns (protoconid and metaconid in the mandibular
777 molars and protocone and paracone in the maxillary molars). We assessed enamel
778 thickness from virtual 2D mesial cross-section planes in each PYS molar as described
779 in Martin (1985)[87] using Amira (6.2, FEI Inc.) and ImageJ (1.51, NIH). In each mesial
780 plane, we measured the enamel (c) and dentine cap (b, including the pulp) areas (in
781 mm^2), adding up into the total crown area (a, in mm^2), and the enamel-dentine
782 junction (EDJ) length (d, in mm). We calculated the average enamel thickness
783 (AET=c/d), the relative enamel thickness (RET= $100*AET/(b^{1/2})$) and the percentage
784 of dentine and pulp in the molar crown (b/a=100*b/a in %). We assessed volume
785 enamel thickness of the molar caps in the complete sample from PYS. Using Amira
786 (6.3.0, FEI Inc.) we performed the segmentation of the dental tissues (enamel, dentine
787 and pulp). We used the semiautomatic tool, threshold-based segmentation, and
788 manual corrections. We employed the protocol of Olejniczak et al. (2008)[86] for the
789 definition of the cervical plane. That is, the plane halfway between the most apical
790 continuous ring of enamel and the plane containing the last hint of enamel. The
791 following variables were measured and/or calculated: volume of the enamel (Ve in
792 mm3); volume of the coronal dentine including the pulp enclosed in the crown (Vcdp
793 in mm3); total volume of the crown, including the enamel, dentine and pulp (Vc in

794 mm3); surface of the EDJ (SEDJ in mm2); percentage of dentine and pulp in the total
795 crown volume (Vcdp/Vc =100*Vcdp/Vc in %); 3D average enamel thickness (3D
796 AET=Ve/SEDJ in mm) and, 3D relative enamel thickness (3D RET=100*3D
797 AET/(Vcdp1/3) a scale-free measurement)[86,88]. In order to extract the largest amount
798 of information of the PYS specimens and the comparative sample, including the
799 occlusal worn molars, we assessed lateral (non-occlusal) enamel thickness in the
800 complete sample. In Amira (6.3.0, FEI Inc.) we defined the occlusal basin plane, a
801 plane parallel to the cervical plane and tangent to the lowest enamel point of the
802 occlusal basin. All material above the occlusal basin plane was removed and only the
803 enamel, dentine and pulp between these two planes were measured[89,90]. The following
804 variables were measured and/or calculated: lateral volume of the enamel (LVe in
805 mm3); lateral volume of the coronal dentine including the pulp enclosed in the crown
806 (LVcdp in mm3); total lateral volume of the crown, including the lateral enamel,
807 dentine and pulp (LVc in mm3); lateral surface of the EDJ (LSEDJ in mm2);
808 percentage of dentine and pulp in the lateral crown volume
809 (LVcdp/LVc=100*LVcdp/LVc in %); 3D average enamel thickness (3D
810 LAET=LVe/LSEDJ in mm) and, 3D lateral relative enamel thickness (3D
811 LRET=100*3D LAET/(LVcdp1/3) a scale-free measurement)[91]. The results of the 2D
812 and 3D measurements in PYS specimens were compared with two populations,
813 Neanderthals and modern humans (MH). Adjusted Z-scores[92,93] of the three variables
814 accounting for tissue proportions (percentage of dentine, AET and RET) were
815 computed to compare 2D and 3D values of the PYS specimens to the means and
816 standard deviations of the Neanderthal and MH groups. This statistical method allows
817 the comparison of unbalanced samples by using Student's inverse t distribution. In
818 these Z-scores the -1.0 to +1.0 interval comprises the 95% of the variation in the

819 reference sample. In addition, standard box and whisker plots were computed to
820 represent three set of variables of crown volume and lateral volume (including 3D
821 Vcdp/Vc, 3D AET, 3D RET and 3D LVcdp/Vc, 3D LAET, 3D LRET) in the PYS
822 sample and the complete comparative specimens and/or groups.
823 **Tissue distribution (cartographic maps)**. In order to visualize enamel thickness
824 topographic distribution in PYS specimens, 3D chromatic maps were generated in
825 Amira (6.3.0, FEI Inc.). The defined chromatic scale is from thinnest (blue) to
826 thickest (red)[94,95]. For comparative purposes, we generated the chromatic maps of a
827 selected sample of specimens, including: Neanderthals from Roc de Marsal (lower
828 and upper deciduous m2), La Quina (upper permanent M1) and Abri Suard (lower
829 permanent M1). Fossil *H. sapiens* from La Madaleine (lower deciduous m2), Qafzeh
830 (upper deciduous m2 and upper and lower permanent M1). And, modern humans
831 from European origin (upper and lower deciduous m2, and upper and lower
832 permanent M1).
833 **Geometric morphometric of the EDJ**. We performed the Geometric morphometric
834 (GM) analysis of the EDJ morphology on the virtual surfaces of PYS specimens and a
835 comparative sample that included Neanderthals, fossil *H. sapiens* and modern humans
836 (Supplementary Information F Table 4). We reconstructed the slightly worn dentine
837 horns of the comparative sample in Geomagic Studio (version 2012;
838 www.geomagic.com) with the fill-holes tool. When necessary we mirrored the
839 comparative specimens according to the PYS molar type. Using landmark tool in
840 Amira, we placed one landmark on the dentine horn tip of each main cusp (protocone,
841 paracone, metacone and hypocone on maxillary molars, and protoconid, metaconid,
842 hypoconid, entoconid and hypocunulid on mandibular molars). Following, we placed
843 a set of semilandmarks (96 and 95 points in maxillary and mandibular molars

844 respectively) along the marginal crests. In each molar, configuration segments were
845 saved independently. Using the package R, we generated the document containing the
846 coordinate configuration for each molar type. Following, using R package we
847 performed the weighted between-group principal component analysis (bgPCA) based
848 on the Procrustes and deformation-based shape residuals[96]. Finally, we tested for
849 allometry on the landmark-based analyses using the coefficient of determination (R2)
850 of a multiple regression[97], in which the explicative variable is the centroid size and the
851 dependent variables are the bgPC scores[98].
852
853 **Faunal analysis**
854 **Zooarchaeology**
855 Two separate zooarchaeological studies were conducted: N.A. analysed remains from
856 burial fill at the Max Planck Institute for the Science of Human History in Jena, and
857 M.E.P. analysed remains from Trenches 3-4 at the National Museums of Kenya in
858 Nairobi. Access to comparative skeletal material for eastern Africa was distinct in
859 each study, and analytical protocols differed somewhat.
860 **Fauna, burial fill**. For the burial fill (context 809 in Trench 8), all bone fragments
861 were sorted, counted and measured (length, width and thickness) using a digital
862 caliper (Mitutoyo 500–463), regardless of identifiability. The specimens were
863 recorded in detail using codes following a zonation system that allow for the
864 description of fragmentation patterns. All identified fragments were examined for
865 bone surface modifications under a Nikon C-PCN stereomicroscope.
866 **Fauna, Trenches 3-4**. For Trenches 3-4, faunal remains are reported from the
867 following layers and contexts: Layer 17 (contexts 316X, 317Y-Z, 420B-F), Layer 18
868 (422A-C), Layer 19 (423A-D). These remains were weighed and sorted into those

identifiable at least to a minimal level (e.g., mammal limb bone), and those not easily identifiable at any level. For each identified specimen, recorded variables include taxon, element, portion, side, weathering, breakage, and bone surface modifications. Cortical surfaces of all identified specimens were examined with a 20x hand lens under strong oblique light.

Sediment analysis

Two sets of samples were analysed in the framework of this study. The first set comprises sediment samples from archaeological layers and the burial pit. The second set includes reddish micro-agglomerates associated with the child remains.

Sediment analysis from archaeological layers and the burial pit. Two groups of sediment samples were analysed. The first group comprises twenty-four samples of sediment collected during the excavation of Trenches 3 and 8 in 2017 (PYS-2017-200127 to PYS-2017-200153). They come from layers 17, 18 and 19, and were collected at 2 cm depth interval. They do not include sediment from the burial (Supplementary Information G Table 1).

The second group comprises five sediment samples collected close to the human remains (Supplementary Information G Table 2). Three samples, reddish-brown in colour, were retrieved close to the maxilla, the face, and inside the cranial vault. The other two, brownish in colour, were collected close to the occipital bone and the postcranial perimeter. These five samples were retrieved during the excavation of the skeleton at the CENIEH's Conservation and Restoration Laboratory.

The sediments samples were studied at the UMR 5199 PACEA and UMR 5060 IRAMAT/CRP2A laboratories in Bordeaux, France. The samples were examined and photographed with a motorised Leica Z6 APOA microscope equipped with a DFC420

digital camera. Uploaded images were treated with Leica Application Suite (LAS) equipped with the Multifocus module. Samples were then prepared for grain-size analysis with a Horiba LA-950 laser particle size analyser. The sample pre-treatment included suspension in sodium hexametaphosphate (5 g/l) and hydrogen peroxide (35%) at room temperature for 12 h. The resulting compound was subjected to 60 s ultrasonification to achieve optimal dispersion. The Mie solution to Maxwell's equation provided the basis for calculating the particle size[99,100], using a refractive index of 1.333 for water and 1.55 – 0.01i for the particles. The grain-size distributions expressed in ϕ units were decomposed in different Gaussian populations (parametric curve fitting method) using the mixdist R package[101] to identify the main modes and their relative proportions. The limits used for grain-size classes are as follows: <7 μm (clays), 7–63 μm (silts), 63-2000 μm (sands). They are based on studies showing that the amount of clay particles measured by laser diffraction is usually underestimated (e.g. Konert and Vandenberghe, 1997[102]).

Elemental analysis was carried out by using a hand-held SPECTRO xSORT energy dispersive X-ray fluorescence (EDXRF) spectrometer from Ametek. This instrument is equipped with a silicon drift detector (SDD), a low power W X-ray tube with an excitation source of 40 kV, and an X-ray beam of 8 mm. Spectra acquisition times were set to 300 s. Measurements were performed with a constant working distance by using a positioning device consisting of a lead receptacle to which the spectrometer was fixed. Samples were previously ground and homogenized with an agate mortar and then placed into a plastic cup covered with a Prolene® thin film. Three measurements were taken on each sample. Element contents were calculated as the average of these acquisitions. In order to precisely quantify the elemental composition of the samples a dedicated calibration for sediment samples was applied (see Sitzia et

al., 2019[103] for details). This calibration allows quantifying Si, K, Ca, Ti, V, Cr, Mn, Fe, Ni, Zn, Ga, As, Rb, Sr, Y, Zr, and Ba. Centred log ratio (*clr*) was used to analyse geochemical data as an alternative to the raw percentages, following Aitchison (1986)[104]. Prior to statistical analysis, a non-parametric replacement was made for the null values below the limit of detection, according to the method proposed by Martín-Fernández et al. (2003)[105]. Some elements were excluded when they displayed more than one third of missing values (Cr, Ni, Sr) or showed a heterogeneous distribution (V). We performed principal component analysis (PCA) of EDXRF concentrations for the thirteen major, minor, and trace elements more frequently detected (Si, K, Ca, Ti, Mn, Fe, Zn, Ga, As, Rb, Y, Zr, Ba). All data analyses were done with the *ade4* package[106] for R software.

We performed XRD analyses on powder samples by using a Bruker D8 Advance diffractometer (Bragg-Brentano Theta-Theta geometry, fixed sample in the horizontal plane, movable tube and detector), goniometer diameter 600mm, Cu anti-cathode X source, Cu-Kα incident X incident doublet radiation. Acquisitions were conducted with an angular range of 3-60° at 2Θ (reticular distances 1.54-29 Å), measurement step 0.01°, a 181px linear detector type Bruker LynxEye covering simultaneously 2.6 ° in 2Θ, an analysis time per point of 550 s (approx. 9 min/px), an angular reproducibility of 0.017°, supporting samples holders of 25 mm in diameter and 1.5 mm thickness, made of PolyMethyl MethAcrylate (PMMA) holders. Samples were previously ground and homogenized with an agate mortar. The time of analysis was 5 h. Mineralogical phases and the semi-quantitative analysis were achieved by using the routine DIFFRAC.SUITE™ EVA software package (Bruker AXS GmbH, Germany) which allows mathematical deletion of bottom noise and Cu-Kα2 component,

combined with the specific powder diffraction file (PDF2) database (International Centre for Diffraction Data—ICDD, Pennsylvania, USA).

Reddish micro-agglomerates associated with the child remains

The reddish micro-agglomerates, possibly fragments of iron-rich rocks commonly called ochre, were detected in the sediment coating the child remains during their excavation and consolidation at the CENIEH. An analytical pipeline involving observation and sampling under low-magnification optical microscope, Raman spectroscopy, X-ray Diffraction (XRD) and Scanning Electron Microscopy coupled with Energy Dispersive X-Ray Spectroscopy (SEM-EDS), was applied to establish the elemental and mineralogical composition of these micro-agglomerates. The aim was to investigate whether ochre may have been involved in the mortuary practices that have led to the deposition and preservation of the child remains. All analyses were conducted at the CENIEH Archaeometry and Microscopy laboratories.

Two groups of reddish micro-agglomerates were analysed. The first set consists of 55 micro-agglomerates contained in samples of reddish-brown clay sediment collected close to the maxillary, the face, and inside the cranial vault. The micro-agglomerates typically correspond to ~900x600 μm associations of grains featuring distinct reddish shades (Supplementary Information G Figure 1). The second group is composed of two larger –~2-10 mm– red fragments collected on the ribs and vertebral bodies (Supplementary Information G Figure 2). Fifteen agglomerates from the first group and the two composing the second group were submitted to analytical microscopy (Raman spectroscopy, SEM-EDS) and XRD analysis (Supplementary Information G Table 3).

966 A FEI Quanta 600 SEM fitted with EDS, and Oxford Instruments INCA software to
967 interface with the EDS, was used to obtain an estimation of the bulk elemental
968 composition of the agglomerates. Operating conditions were 15kV of acceleration
969 voltage, working distance of 10 mm, and acquisition time of 90 seconds, resulting in
970 typical dead times between 10 and 17 %. Unless otherwise specified, results are given
971 as compound weight %, oxygen calculated by stoichiometry and normalised to 100%.
972 All SEM micrographs are Low Vacuum Secondary Electron (SE) images.

973 The samples were first observed at low magnification – typically ranging 100-200x –
974 to capture the entire particle (Supplementary Information G Figure 3). Three
975 representative locations were then selected to investigate the samples microstructure
976 at 1200x where surface features and mineral phases were measured. Three areas were
977 analysed at each location to estimate the average bulk chemical composition. Finally,
978 a mapping of the matrix between crystals was conducted at 2400x and compared to
979 the bulk composition obtained at 1200x (Supplementary Information G Figure 4).
980 Occasionally, other magnifications were used to better investigate texture, grain
981 morphology and their relation with elemental composition. Analyses at high
982 magnifications were conducted to avoid potential biases due to surface irregularities
983 and voids. The analytical procedure was adapted from the analysis of similar mineral
984 particles described in Pitarch Martí et al. (2017)[107].

985 The mineralogical composition of the sample was established by XRD. Due to the
986 destructive nature of this technique, these analyses were not performed on
987 agglomerates analysed by SEM-EDS and RAMAN but on residues coming from the
988 same samples. Sediment was hand grounded in an agate mortar with a pestle. The
989 resulting powder was tapped on silicon discs and mounted into stainless steel sample
990 holders. Patterns were collected with a PANalytical X´Pert PRO MPD diffractometer

with CuKα radiation (λ=1.5406 Å) and a solid-state multichannel detector. Each sample was scanned over the 2-theta range 5- 80˚ with a step size of 0.03. The working tension and intensity were 45kV and 40mA respectively, and the time of analysis ranged from 3 to 16 h. Semi-quantitative analysis was performed on the XRD data using the X´Pert High Score software. Due to the small amount of material analysed the results should be regarded as qualitative.

Raman spectra were acquired using a DRX Thermo Scientific Raman dispersive spectrometer, with a laser emitting at 780 nm. The power radiation measured under the Olympus x50 microscope objective was about 0.5 mW-0.8 mW. Acquisitions of about 25 seconds and multiple additions were used. The spectrometer worked in a spectral range from 55 to 3350 cm^{-1}. The calibration of the spectrometer was done with a polystyrene standard (main band: 1000 cm^{-1}). The recorded mineral spectra were contrasted against the RRUFF database library for phase identification[108] as well as Julien et al. (2004)[109], Bellot-Gurlet et al. (2009)[110], Hanesch (2009)[111] and Babay et al. (2015)[112].

References for Methods

46. Guo, Y.-J. *et al.* New ages for the Upper Palaeolithic site of Xibaimaying in the Nihewan Basin, northern China: implications for small-tool and microblade industries in north-east Asia during Marine Isotope Stages 2 and 3. *J. Quat. Sci.* **32**, 540–552 (2017).
47. Li, B., Jacobs, Z. & Roberts, R. G. Validation of the LnTn method for De determination in optical dating of K-feldspar and quartz. *Quat. Geochronol.* **58**, 1–14 (2020).

48. Blegen, N. *et al.* Distal tephras of the eastern Lake Victoria basin, equatorial East Africa: correlations, chronology and a context for early modern humans. *Quat. Sci. Rev.* **122**, 89–111 (2015).

49. Bronk Ramsey, C. Bayesian analysis of radiocarbon dates. *Radiocarbon* **51**, 337–360 (2009).

50. Dabney, J. *et al.* Complete mitochondrial genome sequence of a Middle Pleistocene cave bear reconstructed from ultrashort DNA fragments. *Proc. Natl. Acad. Sci.* **110**, 15758–15763 (2013).

51. Rohland, N., Glocke, I., Aximu-Petri, A. & Meyer, M. Extraction of highly degraded DNA from ancient bones, teeth and sediments for high-throughput sequencing. *Nat. Protoc.* **13**, 2447–2461 (2018).

52. Gansauge, M.-T. *et al.* Single-stranded DNA library preparation from highly degraded DNA using t4 DNA ligase. *Nucleic Acids Res.* **45**, e79 (2017).

53. Kircher, M., Sawyer, S. & Meyer, M. Double indexing overcomes inaccuracies in multiplex sequencing on the Illumina platform. *Nucleic Acids Res.* **40**, e3 (2012).

54. Korlević, P. *et al.* Reducing microbial and human contamination in DNA extractions from ancient bones and teeth. *BioTechniques* **59**, 87–93 (2015).

55. Glocke, I. & Meyer, M. Extending the spectrum of DNA sequences retrieved from ancient bones and teeth. *Genome Res.* **27**, 1230–1237 (2017).

56. Slon, V. *et al.* Mammalian mitochondrial capture, a tool for rapid screening of DNA preservation in faunal and undiagnostic remains, and its application to Middle Pleistocene specimens from Qesem Cave (Israel). *Quat. Int.* **398**, 210–218 (2015).

57. Fu, Q. *et al.* DNA analysis of an early modern human from Tianyuan Cave, China. *Proc. Natl. Acad. Sci.* **110**, 2223–2227 (2013).

58. Maricic, T., Whitten, M. & Pääbo, S. Multiplexed DNA sequence capture of mitochondrial genomes using PCR products. *PLoS One* **5**, e14004 (2010).

59. Renaud, G., Stenzel, U. & Kelso, J. leehom: adaptor trimming and merging for illumina sequencing reads. *Nucleic Acids Res.* **42**, e141 (2014).

60. Altschul, S. F., Gish, W., Miller, W., Myers, E. W. & Lipman, D. J. Basic local alignment search tool. *J. Mol. Biol.* **215**, 403–410 (1990).

61. Huson, D. H., Auch, A. F., Qi, J. & Schuster, S. C. MEGAN analysis of metagenomic data. *Genome Res.* **17**, 377–386 (2007).

62. Slon, V. *et al.* Neandertal and Denisovan DNA from Pleistocene sediments. *Science* **356**, 605–608 (2017).

63. Li, H. & Durbin, R. Fast and accurate short read alignment with Burrows-Wheeler transform. *Bioinformatics* **25**, 1754–1760 (2009).

64. Meyer, M. *et al.* A high-coverage genome sequence from an archaic Denisovan individual. *Science* **338**, 222–226 (2012).

65. Scheuer, L. & Black, S. Development and ageing of the juvenile skeleton. in *Human Osteology: In Archeology and Forensic Science* (eds. Cox, M. & Mays, S.) 9–22 (Cambridge University Press, 2000).

66. Bullock, P. *et al. Handbook for Soil Thin Section Description*. (Waine Research, 1985).

67. Stoops, G. *Guidelines for Analysis and Description of Soil and Regolith Thin Sections*. (Soil Science Society of America, 2003).

68. *Interpretation of Micromorphological Features of Soils and Regoliths*. (Elsevier, 2018).

69. Hollund, H. I. *et al.* What happened here? Bone histology as a tool in decoding the postmortem histories of archaeological bone from Castricum, the Netherlands. *Int. J. Osteoarchaeol.* **22**, 537–548 (2012).
70. Hedges, R. E. M., Millard, A. R. & Pike, A. W. G. Measurements and relationships of diagenetic alteration of bone from three archaeological sites. *J. Archeol. Sci.* **22**, 201–209 (1995).
71. Millard, A. R. The deterioration of bone. in *Handbook of Archaeological Sciences* (eds. Brothwell, D. R. & Pollard, A. M.) 637–674 (Wiley, 2001).
72. Hackett, C. J. Microscopical focal destruction (tunnels) in exhumed human bones. *Med. Sci. Law* **21**, 243–265 (1981).
73. Jans, M. M. E. Microbial bioerosion of bone: a review. in *Current Developments in Bioerosion* (eds. Wisshak, M. & Tapanila, L.) 397–404 (Springer, 2008).
74. Carlsen, O. *Dental Morphology*. (Munksgaard, 1987).
75. Tobias, P. V. *The Skulls, Endocasts and Teeth of Homo habilis*. vol. 4 (Cambridge University Press, 1991).
76. Turner, C. G., Nichol, C. R. & Scott, G. R. Scoring procedures for key morphological traits of the permanent dentition: the Arizona State University dental Anthropology System. in *Advances in Dental Anthropology* (eds. Kelley, M. & Larsen, C.) 13–31 (Wiley-Liss, 1991).
77. Scott, G. R. & Turner, C. G. *The Anthropology of Modern Human Teeth: Dental Morphology and Its Variation in Recent Human Populations*. (Cambridge University Press, 1997).
78. Martinón-Torres, M. *et al.* Dental evidence on the hominin dispersals during the Pleistocene. *Proc. Natl. Acad. Sci.* **104**, 13279–13282 (2007).

79. Martinón-Torres, M. *et al.* Dental remains from Dmanisi (Republic of Georgia): morphological analysis and comparative study. *J. Hum. Evol.* **55**, 249–273 (2008).

80. Martínez de Pinillos, M., Martinón-Torres, M., Martín-Francés, L., Arsuaga, J. L. & Bermúdez de Castro, J. M. Comparative analysis of the trigonid crests patterns in Homo antecessor molars at the enamel and dentine surfaces. *Quat. Int.* **433**, 189–198 (2017).

81. Martinón-Torres, M., Bermúdez de Castro, J. M., Gómez-Robles, A., Prado-Simón, L. & Arsuaga, J. L. Morphological description and comparison of the dental remains from Atapuerca-Sima de los Huesos site (Spain). *J. Hum. Evol.* **62**, 7–58 (2012).

82. Molnar, S. Human tooth wear, tooth function and cultural variability. *Am. J. Phys. Anthropol.* **34**, 175–190 (1971).

83. Lefêvre, J. Etude odontologique des hommes de Muge. *Bull. Mém. Soc. Anthropol. Paris* **10**, 301–333 (1973).

84. Bermúdez de Castro, J. M., Sarmiento, S., Cunha, E., Rosas, A. & Bastir, M. Dental size variation in the Atapuerca-SH Middle Pleistocene hominids. *J. Hum. Evol.* **41**, 195–209 (2001).

85. Bailey, S. E. A morphometric analysis of maxillary molar crowns of Middle-Late Pleistocene hominins. *J. Hum. Evol.* **47**, 183–198 (2004).

86. Olejniczak, A. J. *et al.* Dental tissue proportions and enamel thickness in Neandertal and modern human molars. *J. Hum. Evol.* **55**, 12–23 (2008).

87. Martin, L. Significance of enamel thickness in hominoid evolution. *Nature* **314**, 260–263 (1985).

88. Kono, R. T. Molar enamel thickness and distribution patterns in extant great apes and humans: new insights based on a 3-dimensional whole crown perspective. *Anthropol. Sci.* **112**, 121–146 (2004).
89. Toussaint, M. *et al.* The Neandertal lower right deciduous second molar from Trou de l'Abîme at Couvin, Belgium. *J. Hum. Evol.* **58**, 56–67 (2010).
90. Zanolli, C. *et al.* Is the deciduous/permanent molar enamel thickness ratio a taxon-specific indicator in extant and extinct hominids? *C. R. Palevol* **16**, 702–714 (2017).
91. Olejniczak, A. J. & Grine, F. E. High-resolution measurement of Neandertal tooth enamel thickness by microfocal computed-tomography. *S. Afr. J. Sci.* **101**, 219–220 (2005).
92. Maureille, B., Rougier, H., Houët, F. & Vandermeersch, B. Les dents inférieures du Néandertalien Regourdou 1 (site de Regourdou, commune de Montignac, Dordogne): analyses métriques et comparatives. *Paleo* **13**, 183–200 (2001).
93. Scolan, H., Santos, F., Tillier, A.-M., Maureille, B. & Quintard, A. Des nouveaus vestiges Néanderthaliens à Las Pélénos (Monsempron-Libos, Lot-et-Garonne, France). *Bull. Mém. Soc. Anthropol. Paris* **24**, 69–95 (2012).
94. Bayle, P. *et al.* Three-dimensional imaging and quantitative characterisation of human fossil remains - examples from the NESPOS database. in *Pleistocene Databases: Acquisition, Storing, Sharing* (eds. Macchiarelli, R. & Weniger, G. C.) 29–46 (Mettmann: Wissenschaftliche Schriften des Neanderthal Museums 4, 2011).
95. Macchiarelli, R., Bondioli, L., Mazurier, A. & Zanolli, C. Virtual dentitions: touching the hidden evidence. in *Technique and Application in Dental*

Anthropology (eds. Irish, J. D. & Nelson, G. C.) 425–448 (Cambridge University Press, 2008).

96. Mitteroecker, P. & Bookstein, F. Linear discrimination, ordination, and the visualization of selection gradients in modern morphometrics. *Evol. Biol.* **38**, 100–114 (2011).

97. Bookstein, F. *Morphometric Tools for Landmark Data Geometric and Biology*. (Cambridge University Press, 1991).

98. Mitteroecker, P., Gunz, P., Windhager, S. & Schaefer, K. A brief review of shape, form, and allometry in geometric morphometrics, with applications to human facial morphology. *Hystrix* **24**, 59–66 (2013).

99. ISO. *Particle size analysis - Laser diffraction methods, Part 1: General principles, Annex A: Theoretical background of laser diffraction*. (2009).

100. Jones, R. M. Particle size analysis by laser diffraction: ISO 13320, standard operating procedures, and mie theory. *Am. Lab.* **35**, 44–47 (2003).

101. Macdonald, P. & Du, J. *Mixdist: Finite mixture distribution models*. (2012).

102. Konert, M. & Vandenberghe, J. Comparison of laser grain size analysis with pipette and sieve analysis: A solution for the underestimation of the clay fraction. *Sedimentology* **44**, 523–535 (1997).

103. Sitzia, L., Gayo, E. M. & de Pol-Holz, R. A perched, high-elevation wetland complex in the Atacama Desert (northern Chile) and its implications for past human settlement. *Quat. Res.* **92**, 33–52 (2019).

104. Aitchison, J. *The Statistical Analysis of Compositional Data*. (Chapman and Hall, 1986).

105. Martín-Fernández, J. A., Barcelo-Vidal, C. & Pawlowsky-Glahn, V. Dealing with zeros and missing values in compositional data sets using nonparametric imputation. *Math. Geol.* **35**, 253–278 (2003).
106. Dray, S. & Dufour, A.-B. The ade4 package: implementing the duality diagram for ecologists. *J. Stat. Soft.* **22**, (2007).
107. Pitarch Martí, A., Wei, Y., Gao, X., Chen, F. & d'Errico, F. The earliest evidence of coloured ornaments in China: the ochred ostrich eggshell beads from Shuidonggou Locality 2. *J. Anthropol. Archaeol.* **48**, 102–113 (2017).
108. Downs, R. T. The RRUFF project: An integrated study of the chemistry, crystallography, raman and infrared spectroscopy of minerals. in (2006).
109. Julien, C. M., Massot, M. & Poinsignon, C. Lattice vibrations of manganese oxides. *Spectrochim. Acta A* **60**, 689–700 (2004).
110. Bellot-Gurlet, L. *et al.* Raman studies of corrosion layers formed on archaeological irons in various media. *J. Nano Res.* **8**, 147–156 (2009).
111. Hanesch, M. Raman spectroscopy of iron oxides and (oxy) hydroxides at low laser power and possible applications in environmental magnetic studies. *Geophys.* **177**, 941–948 (2009).
112. Babay, S., Mhiri, T. & Toumi, M. Synthesis, structural and spectroscopic characterizations of maghemite γ-Fe2o3 prepared by one-step coprecipitation route. *J. Mol. Struct.* **1085**, 286–293 (2015).

Acknowledgements Funding for this project was provided by the SEALINKS project under a European Research Council (ERC) grant (no. 206148) and the Max Planck Society (to N.B.). Funding for the hominin analyses was from the Dirección General

de Investigación of the Ministerio de Ciencia, Innovación y Universidades, grant numbers PGC2018-093925-B-C31 and C33 (MCI/AEI/FEDER, UE) and The Leakey Foundation, through the personal support of G. Getty (2013) and D. Crook (2014-2020) to M.M.-T.; analyses were also carried out at the laboratories of the CENIEH-ICTS with the support of the CENIEH staff. E.S. has a Ramón Areces/Atapuerca Foundation postdoctoral grant. L.M.F. is beneficiary of an Atapuerca Foundation postdoctoral grant. S.J.A. and F.D. acknowledge support from the Research Council of Norway, through its Centres of Excellence funding scheme, SFF Centre for Early Sapiens Behaviour (SapienCE) (no. 262618). FD was funded by the ERC grant, TRACSYMBOLS (no. 249587), the Agence Nationale de la Recherche (ANR-10-LABX-52), LaScArBx Cluster of Excellence, and the Talents program of the University of Bordeaux, Initiative d'Excellence. A.P.M. was funded by the Beatriu de Pinós postdoctoral programme (2017 BP-A 00046) of the Government of Catalonia's Secretariat for Universities & Research of the Ministry of Economy and Knowledge. We thank Boniface Kimeu for the extraction of Mtoto in the field, Nick Blegen for conducting the digital work in the field, Ruth Blasco from IPHES, Tarragona for valuable insights about taphonomy, Rebeca García from University of Burgos and Palmira Saladié from IPHES, Tarragona, for assisting in anatomical identifications, Susana Sarmiento from Fundación Atapuerca for the teeth photographs and Michelle O'Reilly from the Max Planck Institute for the Science of Human History for assisting in graphic design. We thank Gedion Musuko and family for permission to excavate the site. Permission to conduct the research was granted by the National Commision for Science, Technology and Innovation Office of the President of the Republic of Kenya through affiliation with the National Museums of Kenya (NMK).

We are grateful for the support of the NMK administration, staff from the preparation and archeology section. and the British Institute in Eastern Africa.

Author contributions N.B., M.D.P and E.N. designed and directed the PYS research; C.S. and J.B. directed the field excavations; M.M.-T., J.M.B.C., J.L.A., E.S., L.M.F analysed the hominin fossil; P.F. conducted the mechanical restoration and conservation of the hominin; E.S. and J.G.G. conducted the virtual restoration and reconstruction of the hominin; F.d'E., N.A., W.A., S.J.A., J.B., A.C., S.D., K.D., F-X. LB., A.A., D.L., N.K., G.M., D.M., J.M., J.M.M. A.P.M., M.E.P., A.Q., S.R., P.R., M.J.S., C.S. and I.S. conducted analytical studies; M.M.-T., M.D.P., F.d'E. and N.B. wrote the paper with contributions of all authors.

Competing interests The authors declare no competing interests.

Additional information

Supplementary Information is available in the online version:

Data availability. The data that support the findings of this study are available from the corresponding authors upon reasonable request.

Correspondence and requests for materials should be addressed to M.M.-T. (maria.martinon@cenieh.es), N.B. (boivin@shh.mpg.de) or M.D.P. (petraglia@shh.mpg.de).

Extended Data Fig. 1. PYS MSA lithics. Above: The relative size of flakes through Layers 18-17 (MSA) and Layer 16 (early LSA) visualized with a violin plot, illustrating the density of values by layer as a continuous distribution. Notice the decrease across Layers 17-16. The flakes recovered from the burial (n=14), shown here with a boxplot, falls within the variation in product weight for the MSA. The boxplot shows the median value for burial lithics at the centre, with two neighbouring

hinges marking the 25th and 75th percentiles. The whiskers (line extensions) plot the distance from the hinge values to the largest and smallest values in the burial dataset, to a maximum distance of 1.5 times the interquartile range (data beyond this range, if present, would have been plotted as individual outlier points).

Extended Data Fig. 2. Bayesian model for the age estimation of PYS. Left: Bayesian model of all available age determinations from PYS, produced using OxCal 4.4.2 and IntCal20. Right: Age estimate of the burial determined using Bayesian model. A full description (OxCal code) of the age model is provided in Supplemental Information C.

Extended Data Fig. 3. Reconstruction of key taphonomic events of Mtoto's burial. The 3D sequence (a,b,c) illustrates the reconstruction of the key taphonomic events affecting the shape and relationship of the head and the spine. **a**, Original right lateral decubitus position of the child in the burial pit. **b**, Lateral compression of the thorax because of the sediment weight; the ribs are flattened but the rib cage does not collapse as it is common in decomposition in filled space (earth grave). **c**, The head dislocates as it is typical in the case of burials with perishable head support. **d**, Ideal reconstruction of Mtoto's original position at the moment of its discovery at the site.

Extended Data Fig. 4: Analysis of sediment from the stratigraphic sequence and the burial pit. a, Particle size ternary diagram indicating the higher content of sand and silt in the burial pit in comparison to the encasing archaeological layers, and in particular Layer 19. **b**, Examples of particle size distribution and multimodal decomposition showing the similarities of sand and silt modes between the burial

samples and samples 137 (base of Layer 17) and 138 (top of Layer 18). **c**, Elemental profiles of sediment from Layers 17, 18, 19 and the burial pit. Element concentrations are expressed in percentages. Data are presented as mean values. Sediment samples from the burial pit display an elemental composition remarkably similar to the three samples identified as an anomaly at the top of Layer 18 and the base of Layer 17. **d**, Results of PCA of the centre log ratio data (selected elements: SiO_2, K_2O, TiO_2, MnO, Fe_2O_3, Zn, Ga, As, Rb, Y, Zr and Ba). Confidence ellipses at 95%. The burial pit samples markedly differ from Layer 19.

Extended Data Fig. 5. Micromorphological and histological analysis. Polarising microscopy (a, c–f) and SEM (g,h) images of bone and sediment from Mtoto's burial and from surrounding contexts (b). **a,** Ferruginous microfacies (MF-fer: here a coarser-grained variant) adhering on cancellous bone. PPL **b,** Small vertebrate bone fragment from ferruginous sediment at the top of layer 18, about 20 cm above Mtoto's skeleton. Note the good histological preservation and longitudinal and transverse fracturing. PPL. **c,** Mtoto's bone fragment. A Fe-oxide-stained calcite crust (Ca) covers the bone surface. A thin zone of non-clouded bone ('HAP' – conventionally 'hydroxyapatite') immediately beneath the bone surface is underlain with clouded, Ca-enriched bone of the mesosteum (CLb). Note the sharp boundary between HAP and CLb (especially at the left side), and the dense non-Wedl bioerosion foci within CLb (linear longitudinal tunnels ca. 45°; budding tunnels [dark spots], attributed to bacteria) and enlarged osteocyte lacunae (smaller dark spots). Double arrow shows two possible Wedl tunnels. PPL. **d,** As in c), but in XPL. The calcitic crust (Ca) comprises two layers: a Fe-oxide-stained, microcrystalline layer, and a latter layer of clear, coarser-crystalline calcite (grey arrow). Birefringent areas within CLb mark

1283 osteons. Note the loss of birefringence in bioerosion foci (e.g. lower right corner). **e,**
1284 Enlarged osteocyte canaliculi and lacunae, possibly due to fungal or fungal+bacteria
1285 action, in clouded, Ca-enriched bone. PPL. **f,** Advanced alteration of putative human
1286 bone (GHI: 2), with small areas of preserved histology, pervasive clouding, fissuring
1287 (e.g. blue arrow), dissolution pores (e.g. green arrow) and Fe and Mn impregnation
1288 (black spots). Note the spatial patterning of bioerosion, with domains of larger,
1289 circular, coalescent non-Wedl (bacterial) MFD (e.g. red arrow) and smaller, more
1290 typical tunnels (budding and linear longitudinal: e.g. white arrow). A crust of calcite
1291 speleothem (grey arrows) encrusts a transverse fracture across the bone. PPL. **g,**
1292 Budding and linear longitudinal tunnels in highly altered bone (area marked with
1293 white arrow in f). Some smaller-scale, spongiform bioerosion is also shown,
1294 surrounded with permineralised rims (white) of redeposited 'hypdoxyapatite' (light-
1295 blue arrows). SEM image. **h,** Periosteum of clouded bone (Cb), encrusted with
1296 carbonate deposits (MF-carb). Larger circular-elliptical pores (blue/turquoise) are
1297 haversian canals. Circles show foci of fine-scale (0.1-1 μm) bacterial bioerosion
1298 within clouded bone. SEM image, with colour temperature filter to enhance
1299 resolution.
1300
1301 **Extended Data Fig. 6. Histological analysis of Mtoto's bone.** Elemental
1302 composition of clouded bone (Cb) and encrusting calcium carbonate precipitate (Cc)
1303 (SEM-EDS image and spectra). The pictured area corresponds to that of Figure 3 c,d,
1304 Diffuse lighter grey areas within the clouded bone may be permineralised rims around
1305 fine-scale (0.1-1 μm) bioerosion foci. Note the variable enrichment in Ca (especially
1306 in Spectrum 21) and the low concentrations of Fe, Al, and Mg in the authigenic Ca-P
1307 phase that makes up the clouded bone. The pervasive recrystallization of the bone

hydroxyapatite into a Ca-enriched, amorphous or cryptocrystalline calcium phosphate appears to be associated with fine-scale bacterial microtunnelling.

Extended Data Fig. 7. PYS Shell analysis. **a**. Fragments of *Achatina* cf. *fulica* found in close association with the child skeleton. Observation of anatomical features allows for a precise identification of the provenance of the fragments on the shell. Fragments PYS-2017-200407 and PYS-2017-200404 come from the area of the body whorl adjacent to the middle portion of the parietal callus. Fragment PYS-2017-200405 must come from a portion of the shell close to that of the previous fragment and may derive from the same individual. Fragment PYS-2017-200406 comes from the middle of the body whorl, on its dorsal aspect. Although anatomically it is compatible with a provenance from the same individual, its very dark colour, suggestive of a higher Mn intake and different texture of the concretion coating its outer surface, indicates it had a different taphonomic history and may derive from a different shell. Fragment PYS-2017-200086.D comes from the middle of the body whorl, on its ventral aspect. **b**. Refitting of fragments PYS-2017-200407 and PYS-2017-200404. The two large fragments refit along an ancient fracture perpendicularly intercepting the shell growth lines. **c**. Modern striations on the inner surface of specimen PYS-2017-200406, probably produced during excavation or cleaning of the fragments. The modern origin of the striations is shown by their random orientation and absence of the thin manganese patina adhering to the inner surface of this specimen. **d.** Micrographs and 3D reconstruction of an area of fragment PYS-2017-200404 outer surface showing two grooves obliquely crossing the decussated sculpture of the outer shell surface. The grooves internal morphology and outline indicate that they were made by a pointed agent, possibly a stone tool, following the irregular morphology of the shell

natural surface and slightly changing direction when falling into concave areas. The antiquity of the lines is demonstrated by the red sediment coating the specimen, which fills in the striations and almost completely bury them when they run into natural grooves of the shell. **e**. Fragments of *Achatina* cf. *fulica* found in feature 809 (bottom) and their anatomical origin (top). The twelve fragments mostly come from *Achatina* snails body whorls and last whorls of the spire, only two from the parietal wall and the apex. They present a similar state of preservation, colour, taphonomic modifications and type of concretions observed on the five fragments found in direct association with the skeleton. None of them bears incisions similar to those recorded on specimen PYS-2017-200404. Fragments comprising the control sample from layer 18 are, in general, more free from concretions than those from the skeleton and feature 809. **f**. Biplot and linear regression correlating the length and width of *Achatina* cf. *fulica* fragments from the grave pit (n=12) and the skeleton (n=5), (Burial with those from layer 18 (n=581) (top), and box plots of length and width distributions of *Achatina* cf. *fulica* fragments from these two contexts (bottom). Rectangles in the boxplots show the second and third quartiles, central bar indicates the median and whiskers extreme values. The fragments from the burial pit are significantly larger in size (p= 0,001) while displaying the same length/width ratio. Incorporation in the grave infilling have preserved *Achatina* fragments from the higher levels of fragmentation that have affected fragments exposed to trampling on the occupation surface in Layer 18.

Extended Data Fig. 8 PYS human dental remains. a, PYS dental remains: isolated teeth (left column) and mCT 3D reconstruction of the two molars included in the maxillary and mandibular bones (right column). All molars are positioned with the mesial surface towards the top and the distal surface towards the bottom. L (left); R

(right); dm2 (second deciduous molar), M^1 (permanent upper first molar), M_1 (permanent lower first molar). **b**, Between-group principal component analysis (bgPCA) of the Procrustes shape coordinates of the PYS Ldm2 enamel dentine-junction surface (EDJ) compared with to those of Neanderthals (n=6), fossil *H. sapiens* (n=3) and modern humans (n=5). **c**, Between-group principal component analysis (bgPCA) of the Procrustes shape coordinates of the PYS RM1 EDJ compared with to those of Neanderthals (n=6), fossil *H. sapiens* (n=2) and modern humans (n=12). **d**, Between-group principal component analysis (bgPCA) of the Procrustes shape coordinates of the PYS RM1 EDJ compared with to those of Neanderthals (n=12), fossil *H. sapiens* (n=3) and modern humans (n=12).

Extended Data Table 1. PYS faunal remains. Fragmentation of the appendicular skeletal elements recorded from the fill close to the burial in Trench 8. The high level of fragmentation of the faunal remains contrasts with the relative completeness but advanced degradation of Mtoto's skeletal remains, indicating different taphonomic histories for faunal and human remains. Fragmentation code: I- <25%, II- >25%-<50%, III->50%-<100%, IV- 100%.

Extended Data Table 2. Diagenesis of identifiable and putative human bone in Mtoto's section. lld: linear-longitudinal MFD; bd: budded MFD; lam: lamellate MFD; HAP: hydroxyapatite; Cc: calcite.

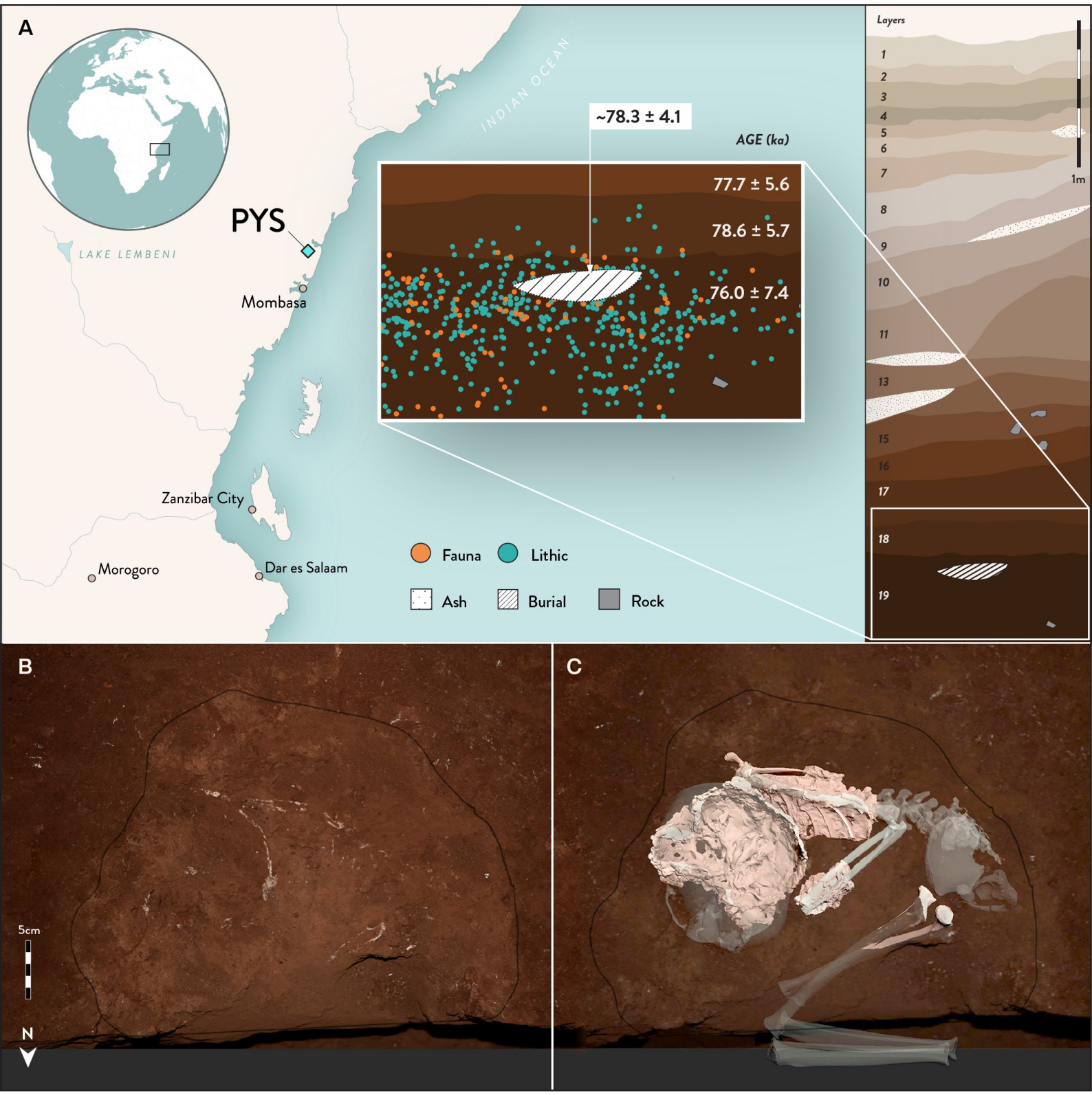
A
INDIAN OCEAN
~78.3 ± 4.1
AGE (ka)
77.7 ± 5.6
78.6 ± 5.7
76.0 ± 7.4
PYS
LAKE LEMBENI
Mombasa
Zanzibar City
Morogoro
Dar es Salaam
Fauna
Lithic
Ash
Burial
Rock
Layers
1
2
3
4
5
6
7
8
9
10
11
13
15
16
17
18
19
1m
B
5cm
N
C

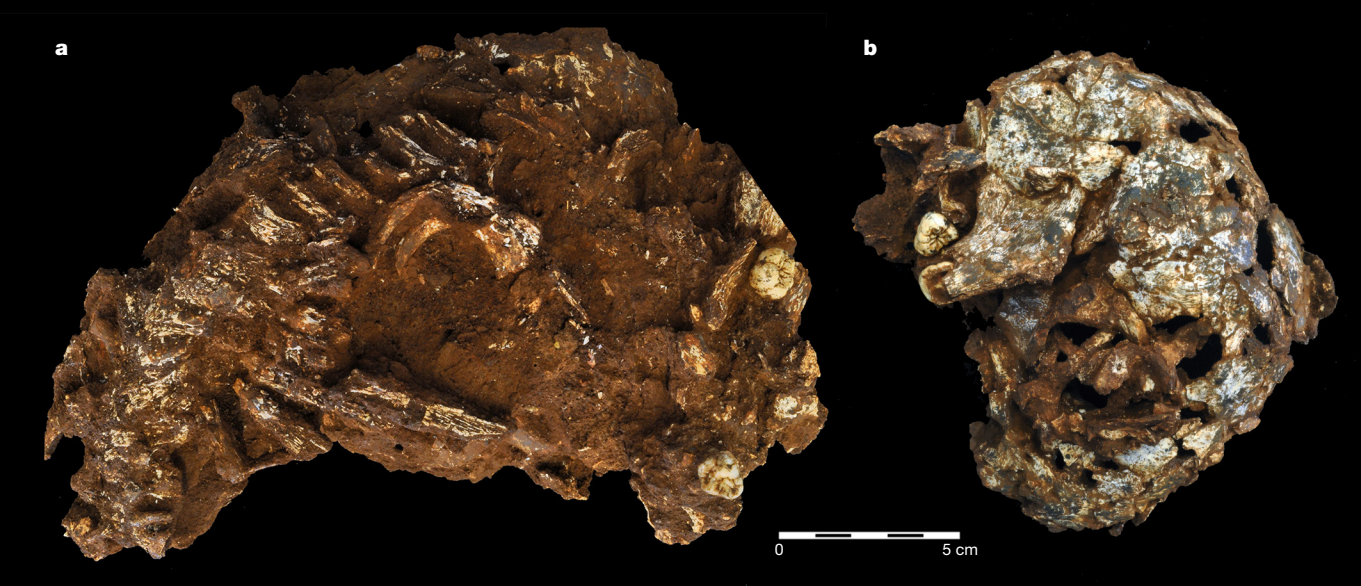
a
b
0
5 cm

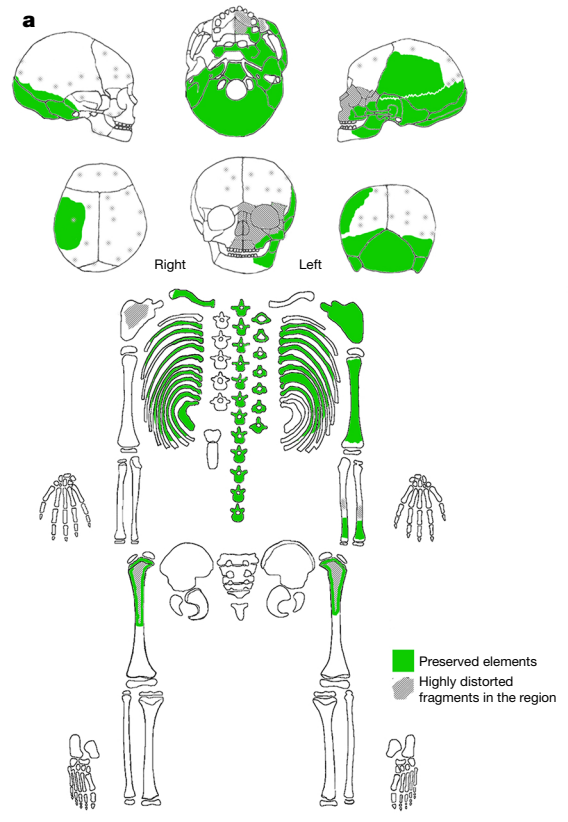
a
Right
Left
Preserved elements
Highly distorted fragments in the region

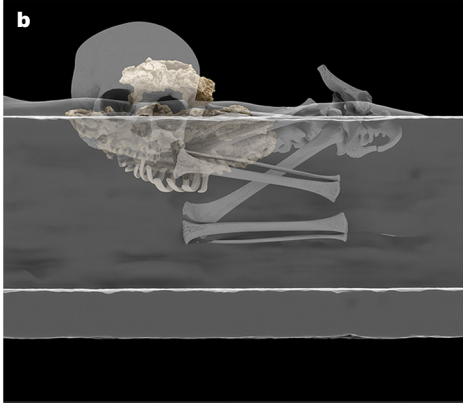
b

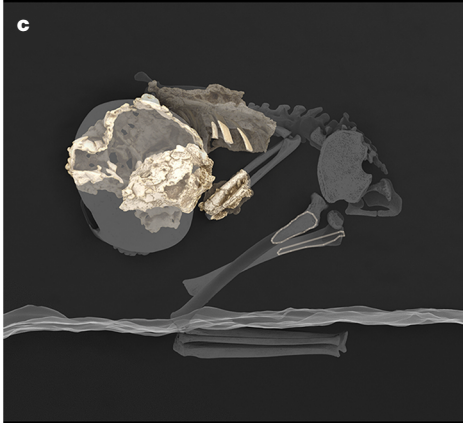
c